SAND2022-17124C

Numerical considerations of slow acoustic mode in high-velocity boundary layers

Shaun R. Harris* and Ross M. Wagnild†
Sandia National Laboratories, Albuquerque, NM 87185

Direct numerical simulations (DNS) were conducted of a high-velocity flat plate boundary layer with time-periodic fluctuating inflow. The DNS fluctuation growth and evolution over the plate is then compared to the solution as computed using classical linear stability theory (LST) and the parabolized stability equations (PSE) of a second mode eigenfunction. The decay rate of the freestream perturbations is also compared to LST and the choice of shock-capturing method and the associated dissipation rate is characterized. The agreement observed between the eigenfunction from LST and the fundamental harmonic of the temporal Fourier transform (FT) of the DNS simulation demonstrates the ability of the solver to capture the initiation and linear growth of a hypersonic boundary layer instability. The work characterizes the shock-capturing numerical dissipation for slow and second mode growth as well as provides confidence in the numerical solver to study further development towards non-linear growth and eventual transition to turbulence.

I. Nomenclature

BL	=	boundary layer
C	=	generic coefficient
δ_{99}	=	99% boundary layer thickness
DNS	=	direct numerical simulation
FT	=	Fourier transform
IO	=	input-output optimization
LST	=	Linear Stability Theory
M	=	Mach number
PSE	=	Parabolized Stability Equations
$\mathbf{q}$	=	state vector of velocities and pressure
$\hat{\mathbf{q}}$	=	Fourier transform coefficient of state vector
RMS	=	root mean square
sdist	=	streamwise distance along the flat plate
SPARC	=	Sandia Parallel Aerodynamics and Reentry Code
STABL	=	Stability and Transition Analysis for hypersonic Boundary Layers
t	=	time (s)
u, v, w	=	streamwise, wall-normal, and spanwise velocities (m/s)
x, y, z	=	streamwise, wall-normal, and spanwise dimensions (m)

II. Introduction

In hypersonic flight, the laminar to turbulent transition has a large impact on the heat transfer across an atmospheric flight vehicle. As is outlined by Federov [1] the transition process changes as freestream disturbances are increased. In the low disturbance environment of flight, eigenmode growth is believed to be the dominant process underlying boundary layer transition. The path to transition shows how eigenmode growth is the dominant mechanism leading to nonlinear breakdown and eventually transition to turbulence. In high-velocity flight conditions, stability theory indicates that Mack's second mode instabilities are often the dominant modes leading to the initial modal interactions. Modeling

*Postdoctoral Appointee, Aerosciences Department, Member AIAA.
†Principal Member of the Technical Staff, Aerosciences Department, Associate Fellow AIAA.

this growth can be done using a combination of linear stability theory (LST) and the parabolized stability equations (PSE). Using these stability methods allows for predictions of the second mode growth and decay in laminar flow with relatively low computational cost. These methods restrict one to pure laminar flow and small amplitude perturbations that do not excite modal interactions or the transition process. In order to calculate the full transition process from laminar to turbulent, one requires a more costly approach such as using direct numerical simulation (DNS). This DNS approach allows for accurately capturing low-amplitude disturbances in a boundary layer and compares well with PSE analysis. Additionally, the DNS approach can capture nonlinear interactions for high-amplitude disturbances and the full transition process to turbulence. Modeling the full transition process will be valuable in understanding the various sensitivities of the transition process in these flow regimes. To gain confidence in the simulation and methods, we turn our attention in this work to the linear and low-amplitude perturbation growth.

In this work we utilize the Sandia Parallel Aerodynamics and Reentry Code (SPARC) [2] on a hypersonic flow condition with perturbation growth in a boundary layer as the DNS solver. SPARC is a "next-generation" transonic and hypersonic CFD code that supports high performance computing and performance portability for a variety of computer architectures including GPU platforms. The software solves either the perfect gas or the reacting gas Navier-Stokes equations and has several discretization methods capable of standard hypersonic numerics as well as low dissipation methods for DNS. For these computations, we are using the perfect gas solver using Sutherland's law for viscosity and a constant Prandtl number for thermal conductivity. The inviscid fluxes were calculated using the kinetic energy conserving fourth order scheme of Subbareddy-Candler [3]. The corresponding experiment uses nitrogen, therefore, the gas simulated in these simulations uses the properties of nitrogen.

For the linear stability analysis, a suite of tools for stability calculations and analysis of hypersonic boundary layers known as Stability and Transition Analysis for hypersonic Boundary Layers (STABL) [4] was utilized. The geometry of interest in these calculations is a simple flat plate that is one meter long. Using STABL, a frequency matching the largest second mode growth is chosen for the specified conditions. The inflow for the DNS cases is then set at this frequency with a uniform in space and time-periodic perturbations. The freestream conditions of the flow over the flat plate hypersonic boundary-layer are shown in Table 1. The wall was treated as isothermal with a temperature of $T_w = 300\ K$.

M_∞ (-)	Re (10^6 1/m)	P_0 (kPa)	T_0 (kelvin)
7.9	13.4	4692.2	617.8

Table 1 Freestream conditions chosen for this study to compare to experiment in Table 1. of [5]. We include the freestream Mach number, the Reynolds number, the stagnation pressure, and the stagnation temperature

This work presents further simulations and results from remaining questions outlined in previous work presented in [6]. It was found in that previous work demonstrated the SPARC solvers ability to capture Mack's second mode growth for various conditions. The simulations in that study demonstrated some remaining transient behavior near the inflow boundary along with some underprediction of the growth using a certain numerical treatment. Both of these behaviors are discussed in further detail in this work.

III. Methods

The outline of the conditions and methods for both LST and DNS for this compressible flow are used to estimate the growth of the second mode eigenvalue in a boundary layer at the specified flow conditions is presented in the following.

A. Baseflow

In order to utilize LST and compute unstable modes, one must obtain a time averaged baseflow. The least expensive approach would be to use a similarity solution [7]. The derivation and description was initially done by [7] and summarized by [8] and is presented in Appendix A. The results from this similarity solution can be compared to the DNS time-averaged solutions that are discussed in greater detail in section IV.A. The exact details of the DNS cases are not vital to the general understanding that the time-averaged solutions from DNS generally agree well with the similarity solution when using a variety of inflow boundary conditions.

The inflow conditions for each case are specified in section IV.A. The density, streamwise velocity, wall-normal velocity, and temperature for the similarity and DNS solutions are shown in Figures 1, 2, 3, and 4. These figures all demonstrate agreement for the flow over the plate at the desired flow conditions using the similarity transformation and

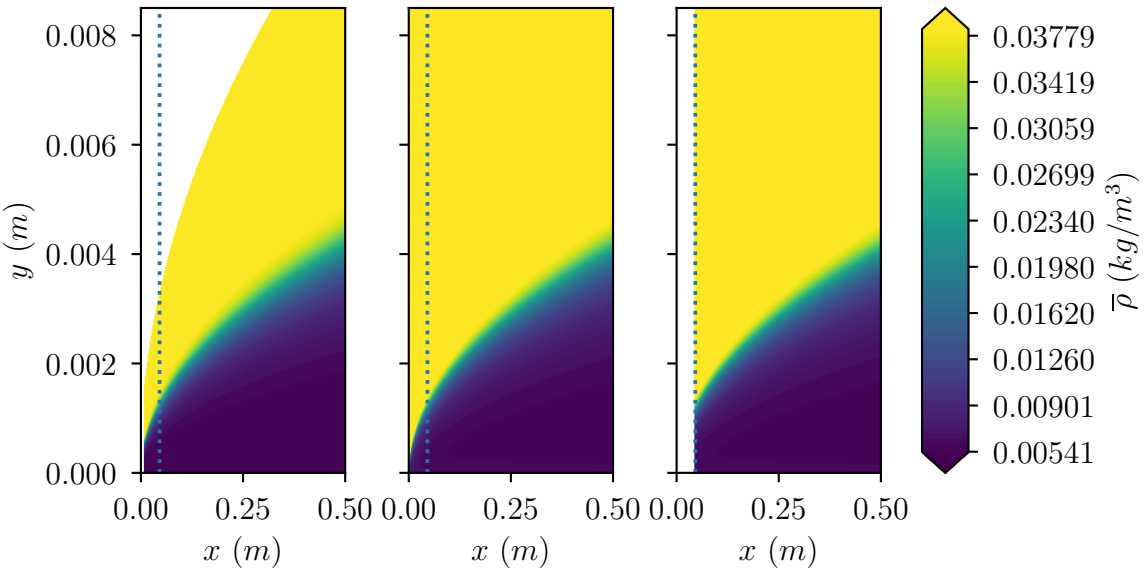

Fig. 1 Density solution over a flat plate at the specified flow conditions from Table 1. Solutions are shown from left to right resulting from the similarity transformation, 2D acoustic inflow DNS case, and 2D BL DNS case. The vertical blue dotted line indicates the inflow condition for the 2D BL DNS at $x = 0.046$.

the DNS with various inflows. There are a few minor differences that can be observed. The laminar flow condition has no information regarding the shock weak shock location, but the STABL and SPARC simulations both contain shock information as observed in Figure 3. The dotted blue lines on the figures designate the $x = 0.046$ streamwise location which is the inflow location for the 2D BL DNS case as well as when the second mode becomes unstable as identified using STABL. Further insight at these locations are presented and discussed in Figures 12-16 and section IV.A.

B. LST and PSE

LST and PSE are popular choices for estimating the eigenmode growth in a boundary layer due to the accuracy afforded and the relatively inexpensive computation. For LST, we assume a locally parallel baseflow and the ansatz,

$$\mathbf{q} = \hat{\mathbf{q}}(y)e^{i(\alpha x+\beta z-\omega t)} + c.c., \tag{1}$$

is substituted into the linearized Navier-Stokes equations where $c.c.$ indicates the complex conjugate. Neglecting non-parallel and nonlinear terms leads to an eigenvalue problem of the form

$$\mathsf{L}\hat{\mathbf{q}} = \alpha\hat{\mathbf{q}}. \tag{2}$$

The specific operators, normalization, and assumptions are discussed and presented by [4, 9] for both the LST and PSE calculations for compressible flows. We solve this eigenvalue problem at a range of frequencies and locations along the plate to get an idea of the expected growth and decay of various modes. Plotting the growth rate (imaginary part of the eigenvalue α) gives the following stability diagram shown in Figure 5. The black dotted line in this figure indicates the maximum growth at 91.21 kHz. The strong growth shown around that frequency range for the majority of the length studies is caused by the second mode instability. Fluctuations in this frequency range tend to see large amplification and in several high-speed flows, this is the dominant eigenmode observed.

PSE relaxes the parallel flow assumption of LST by utilizing a non-parallel baseflow and uses the ansatz

$$\mathbf{q} = \hat{\mathbf{q}}(x, y)e^{i(\int \alpha dx+\beta z-\omega t)} + c.c. \tag{3}$$

Neglecting small and nonlinear terms from the disturbance Navier-Stokes equations we arrive at the PSE that can be marched downstream using an integration technique [10]. It should be noted that the solution procedure is unstable due to remaining ellipticity in the governing equations and a remedy must be used to eliminate the remaining ellipticity.

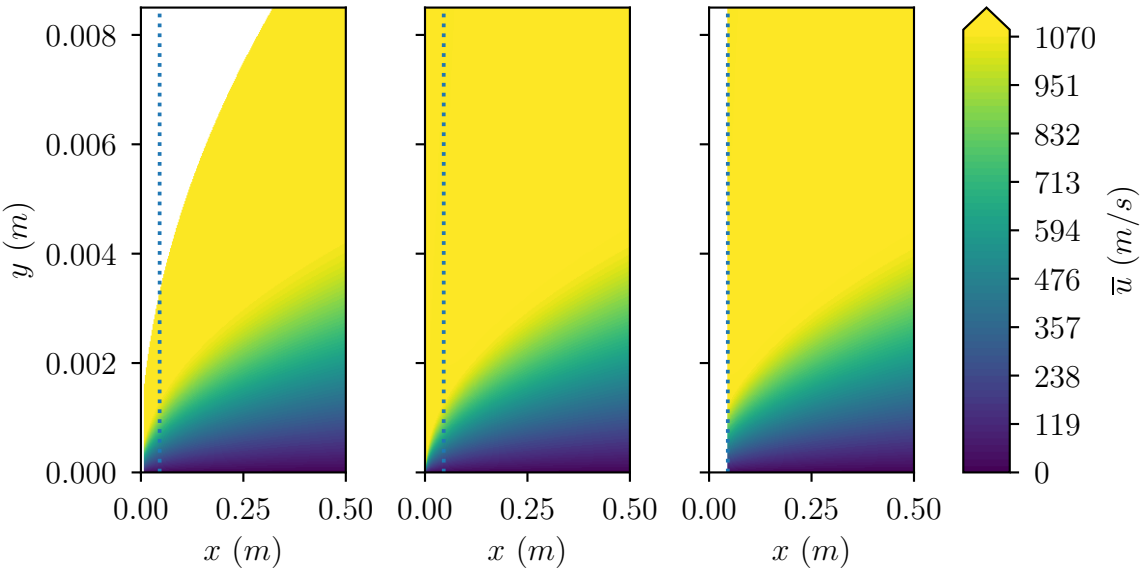

Fig. 2 Streamwise velocity solution over a flat plate at the specified flow conditions from Table 1. Solutions are shown from left to right resulting from the similarity transformation, 2D acoustic inflow DNS case, and 2D BL DNS case. The vertical blue dotted line indicates the inflow condition for the 2D BL DNS at $x = 0.046$.

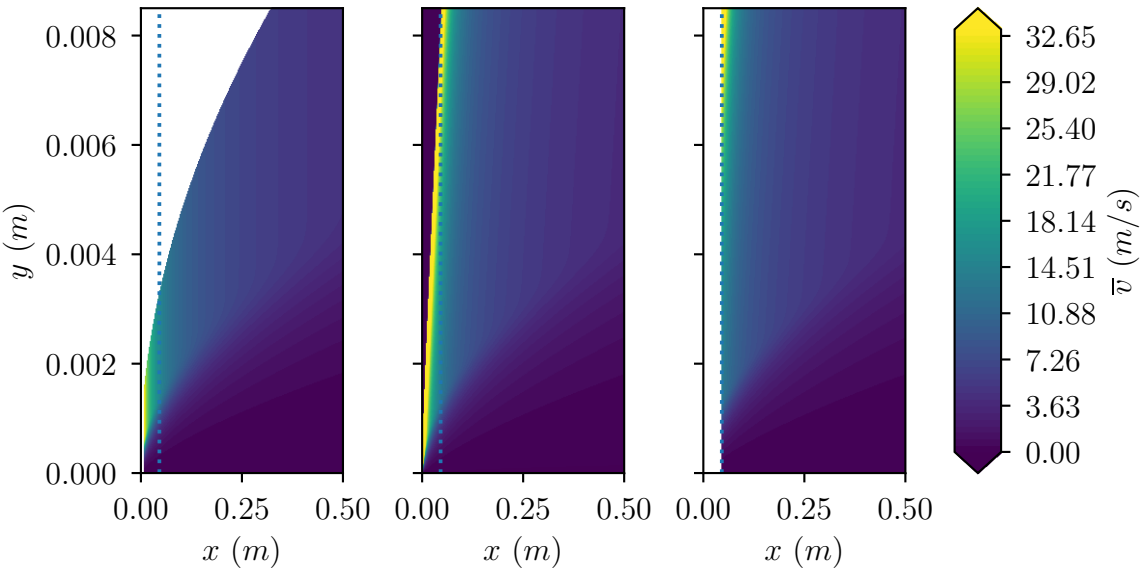

Fig. 3 Wall-normal velocity solution over a flat plate at the specified flow conditions from Table 1. Solutions are shown from left to right resulting from the similarity transformation, 2D acoustic inflow DNS case, and 2D BL DNS case. The vertical blue dotted line indicates the inflow condition for the 2D BL DNS at $x = 0.046$.

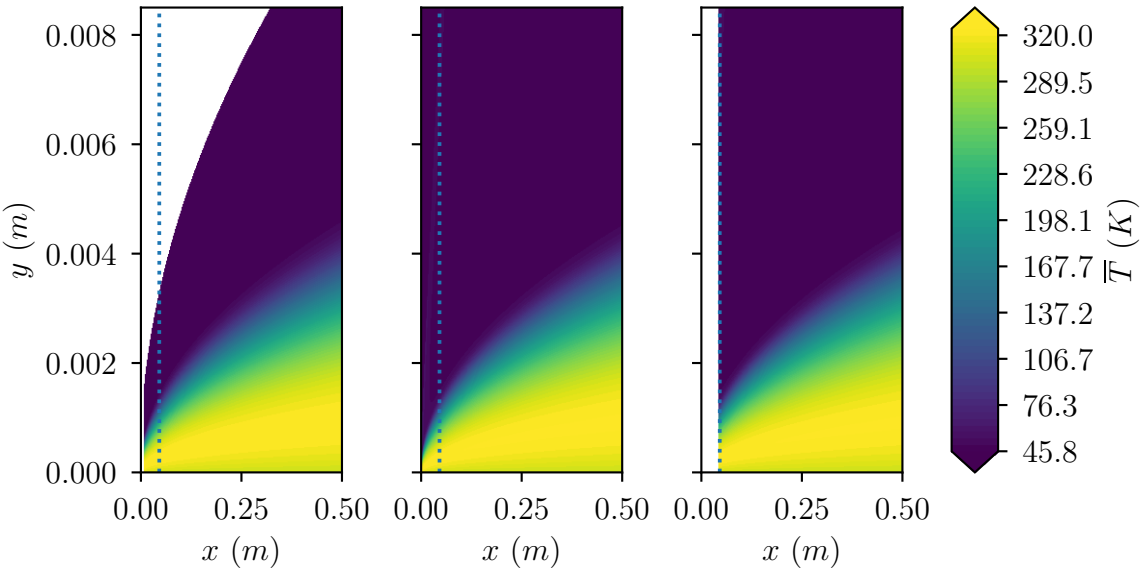

Fig. 4 Temperature solution over a flat plate at the specified flow conditions from Table 1. Solutions are shown from left to right resulting from the similarity transformation, 2D acoustic inflow DNS case, and 2D BL DNS case. The vertical blue dotted line indicates the inflow condition for the 2D BL DNS at x = 0.046.

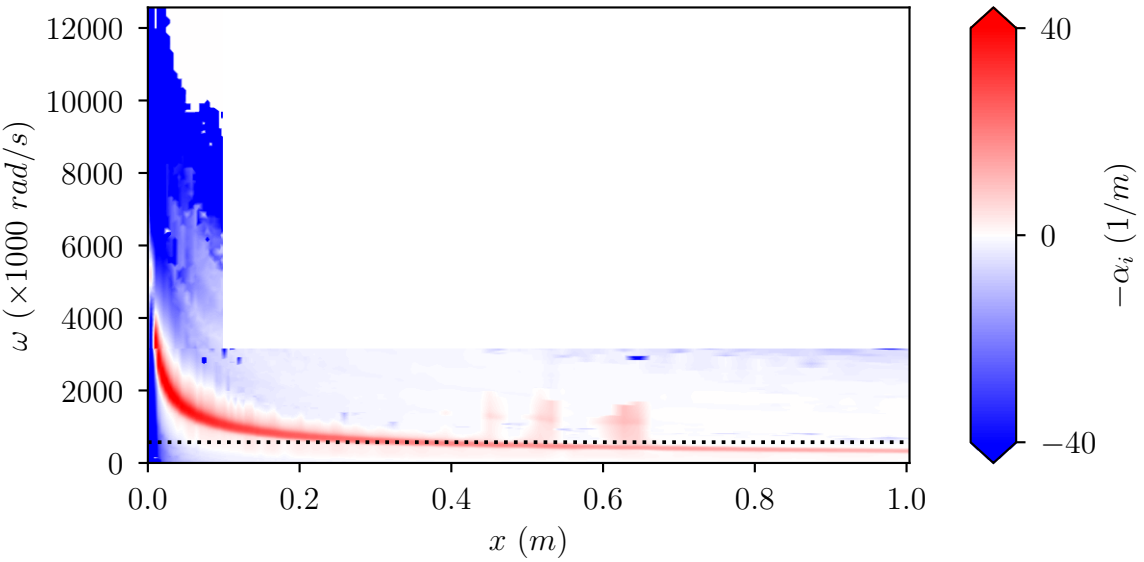

Fig. 5 STABL stability diagram for the given flight conditions. The black dotted line indicates the maximum growth at 91.21 kHz over the domain.

A summary of these possible remedies can be found in [11]. Of the possible remedies suggested there, STABL uses the pressure gradient suppression to stabilize the marching procedure. The PSE are used to march the eigenfunctions identified in the LST analysis downstream and the mode with the largest overall growth is identified. The resulting LST values near the leading edge of the plate is presented in Table 2.

x (m)	α (rad/m)	β (1/m)	$f = \frac{\omega}{2\pi}$ (kHz)
0.05	591.2 + 3.4i	0	91.2

Table 2 STABL parameters of the second mode instability. At the initial location the mode is stable.

1. Freestream LST

In a calorically perfect ideal gas, the compressible nondimensional Navier-Stokes equations are simplified and re-arranged following the derivation by [12]. The equations become

$$\frac{D\rho}{Dt} + \rho\nabla\cdot\boldsymbol{u} = 0, \tag{4}$$

$$\rho\frac{D\boldsymbol{u}}{Dt} + \nabla p = \frac{1}{\mathrm{Re}}\nabla\cdot\boldsymbol{\tau}, \tag{5}$$

$$\rho\frac{DT}{Dt} + M^2\gamma(\gamma-1)p\nabla\cdot\boldsymbol{u} = \frac{\gamma(\gamma-1)M^2}{Re}\nabla\boldsymbol{u} : \boldsymbol{\tau} - \frac{\gamma}{\mathrm{PrRe}}\nabla\cdot\boldsymbol{q}, \tag{6}$$

where Pr is the Prandtl number, γ is the ratio of specific heats, and Re is the Reynolds number based on plate length L. The heat flux vector $\boldsymbol{q}$ and the viscous stress tensor components are defined as

$$q_i = -k\frac{\partial T}{\partial x_i}, \tag{7}$$

and

$$\tau_{ij} = \mu\left(\frac{\partial u_i}{\partial x_j}\right). \tag{8}$$

We also implement the ideal gas equation of state as $p = \rho RT$ to close the system.

If we then introduce an ansatz for the two-dimensional primitive variables,

$$\begin{bmatrix}\rho\\ u\\ v\\ T\end{bmatrix} = \begin{bmatrix}\overline{\rho}\\ \overline{u}\\ \overline{v}\\ \overline{T}\end{bmatrix} + \left(\begin{bmatrix}\hat{\rho}\\ \hat{u}\\ \hat{v}\\ \hat{T}\end{bmatrix} e^{i(\alpha x+\lambda y-\omega t)} + c.c.\right) \tag{9}$$

we can further neglect nonlinear disturbance terms and viscous quantities to obtain the linearized Euler equations in operator form as

$$\begin{bmatrix}\Delta & \alpha\overline{\rho} & \lambda\overline{\rho} & 0\\ \frac{\alpha R\overline{T}}{\overline{\rho}} & \Delta & 0 & \alpha R\\ \frac{\lambda R\overline{T}}{\overline{\rho}} & 0 & \Delta & \lambda R\\ 0 & \alpha\overline{T}(\gamma-1) & \lambda\overline{T}(\gamma-1) & \Delta\end{bmatrix}\begin{bmatrix}\hat{\rho}\\ \hat{u}\\ \hat{v}\\ \hat{T}\end{bmatrix} = 0 \tag{10}$$

where $\Delta = \alpha\overline{u} + \lambda\overline{v} - \omega$. Here, the bar indicates time and spatial averaged constant quantities. Rearranging this to solve for the temporal eigenvalue problem gives the equation

$$\begin{bmatrix}\alpha\overline{u}+\lambda\overline{v} & \alpha\overline{\rho} & \lambda\overline{\rho} & 0\\ \frac{\alpha R\overline{T}}{\overline{\rho}} & \alpha\overline{u}+\lambda\overline{v} & 0 & \alpha R\\ \frac{\lambda R\overline{T}}{\overline{\rho}} & 0 & \alpha\overline{u}+\lambda\overline{v} & \lambda R\\ 0 & \alpha\overline{T}(\gamma-1) & \lambda\overline{T}(\gamma-1) & \alpha\overline{u}+\lambda\overline{v}\end{bmatrix}\begin{bmatrix}\hat{\rho}\\ \hat{u}\\ \hat{v}\\ \hat{T}\end{bmatrix} = \omega\begin{bmatrix}\hat{\rho}\\ \hat{u}\\ \hat{v}\\ \hat{T}\end{bmatrix} \tag{11}$$

The resulting eigenvalue/eigenfunction pairs results in four waves. The vorticity and entropy waves are identified by non-zero components of the eigenfunctions, $\boldsymbol{\xi}_1$ and $\boldsymbol{\xi}_2$, and the slow and fast acoustic waves are identified by the magnitude of the eigenvalues, ω_3 and ω_4. The four eigenvalue/eigenfunction pairs are

$$\omega_1 = \alpha\overline{u} + \lambda\overline{v}, \quad \boldsymbol{\xi}_1 = \begin{bmatrix} 0 \\ -\lambda \\ \alpha \\ 0 \end{bmatrix}, \tag{12a}$$

$$\omega_2 = \alpha\overline{u} + \lambda\overline{v}, \quad \boldsymbol{\xi}_2 = \begin{bmatrix} -\overline{\rho} \\ 0 \\ 0 \\ \overline{T} \end{bmatrix}, \tag{12b}$$

$$\omega_3 = \alpha\overline{u} + \lambda\overline{v} - a\sqrt{\alpha^2+\lambda^2}, \quad \boldsymbol{\xi}_3 = \begin{bmatrix} \overline{\rho} \\ -\frac{\alpha a}{\sqrt{\alpha^2+\lambda^2}} \\ -\frac{\lambda a}{\sqrt{\alpha^2+\lambda^2}} \\ \overline{T}(\gamma-1) \end{bmatrix}, \tag{12c}$$

and

$$\omega_4 = \alpha\overline{u} + \lambda\overline{v} + a\sqrt{\alpha^2+\lambda^2}, \quad \boldsymbol{\xi}_4 = \begin{bmatrix} \overline{\rho} \\ \frac{\alpha a}{\sqrt{\alpha^2+\lambda^2}} \\ \frac{\lambda a}{\sqrt{\alpha^2+\lambda^2}} \\ \overline{T}(\gamma-1) \end{bmatrix}. \tag{12d}$$

Here, a is the speed of sound in the baseflow.

If we further assume that the baseflow is aligned with the streamwise direction, $\overline{v} = 0$, and that the wave is independent of the y direction, $\lambda = 0$, then the eigenvalues and eigenfunctions become

$$\omega_1 = \alpha\overline{u}, \quad \boldsymbol{\xi}_1 = \begin{bmatrix} 0 \\ 0 \\ \alpha \\ 0 \end{bmatrix} \tag{13a}$$

$$\omega_2 = \alpha\overline{u}, \quad \boldsymbol{\xi}_2 = \begin{bmatrix} -\overline{\rho} \\ 0 \\ 0 \\ \overline{T} \end{bmatrix} \tag{13b}$$

$$\omega_3 = \alpha(\overline{u} - a), \quad \boldsymbol{\xi}_3 = \begin{bmatrix} \overline{\rho} \\ -a \\ 0 \\ \overline{T}(\gamma-1) \end{bmatrix} \tag{13c}$$

$$\omega_4 = \alpha(\overline{u} + a), \quad \boldsymbol{\xi}_4 = \begin{bmatrix} \overline{\rho} \\ a \\ 0 \\ \overline{T}(\gamma-1) \end{bmatrix} \tag{13d}$$

It should be noted, that for the linearized Euler equations, that the phase velocity is completely real valued, thus there is no decay existing in the system. Therefore, the disturbances would continue on without any decay or growth in time or

space. For high Reynolds number flows, this type of assumption is fairly accurate, as these waves decay very slowly. As Reynolds numbers become lower, viscous effects become more pronounced and the decay rate is more observable for the disturbance waves. For the flat plate, we observe small decay rates due to the high Reynolds numbers associated with this flow of interest.

If we allow the viscous terms to remain in the system, we obtain the operator form of the governing equations and the resulting eigenvalue problem with the additional terms

$$\begin{bmatrix} \Delta & \alpha\overline{\rho} & \lambda\overline{\rho} & 0 \\ \frac{\alpha R\overline{T}}{\overline{\rho}} & \Delta - \frac{i\mu}{\overline{\rho}}\left(\frac{4}{3}\alpha^2 + \lambda^2\right) & 0 & \alpha R \\ \frac{\lambda R\overline{T}}{\overline{\rho}} & 0 & \Delta - \frac{i\mu}{\overline{\rho}}\left(\alpha^2 + \frac{4}{3}\lambda^2\right) & \lambda R \\ 0 & \alpha\overline{T}(\gamma-1) & \lambda\overline{T}(\gamma-1) & \Delta - \frac{ik}{\overline{\rho}c_v}\left(\alpha^2+\lambda^2\right) \end{bmatrix} \begin{bmatrix} \hat{\rho} \\ \hat{u} \\ \hat{v} \\ \hat{T} \end{bmatrix} = \omega \begin{bmatrix} \hat{\rho} \\ \hat{u} \\ \hat{v} \\ \hat{T} \end{bmatrix} \tag{14}$$

where $\Delta = \alpha\overline{u} + \lambda\overline{v}$, k is the thermal conductivity, c_v is the specific heat at constant volume, and i is the imaginary number. Solving this eigenvalue problem leads to complex valued eigenvalues and eigenfunctions and is typically solved numerically. For high Reynolds number flows, the complex valued eigenvalues are similar to the inviscid counterparts, but they do contain imaginary component indicating decay over time as the mode is carried downstream at the specific phase velocity. This viscous linear stability theory for freestream modes is used in comparison to the DNS results.

C. DNS

One major focus of this work is to validate the SPARC solver's ability to calculate the linear growth of the second mode instability present at these flow conditions. Therefore, SPARC was used to mimic the PSE process by calculating the same flow conditions with a fluctuating inlet of different types. A series of case studies each with separate simulations are presented with varying boundary conditions and complexity.

The first simulation type, referenced by the term acoustic, contains a single uniform acoustic perturbation given ahead of the flat plate. The acoustic forcing inlet in SPARC is used for the first calculation and is outlined in [6]. This uses the freestream eigenvalues and eigenfunctions for a slow acoustic mode as the inlet condition. The mesh contained 10.1 million control volumes and was made two-dimensional by making the spanwise periodic dimension only two cells wide. This type of two-dimensional spanwise treatment is used for all cases that are labeled 2D.

The second simulation type consisted of a smaller domain where the inflow was altered to match the second mode eigenfunction and matching frequency identified from STABL with the respective boundary layer. This reduced the computational expense by decreasing the number of control volumes to roughly 5.4 million for the two-dimensional grid. This simulation grid was used in several separate simulations with varying inlet profiles and streamwise locations and were presented previously in [6]. One case study investigated one point just beyond the start of the leading edge of the plate with varying magnitude of the perturbation. This location lies just before the neutral point in the LST modal growth and corresponds to the values in Table 2. This case study provided confidence for SPARC to capture the linear growth using these inflow conditions as well as observe some initial nonlinear growth.

The third domain started downstream of the neutral point, and contained significant spanwise resolution. The increased resolution was used to validate the three-dimensional capability to capture the linear growth of the two-dimensional eigenmode and matching growth. This grid contained roughly 679 million control volumes.

All domains consisted of a rectangular volume discretized using rectangular finite volumes. To ensure accuracy of the calculation, the grid was clustered to the wall with a $\Delta y^+ = 1$ chosen in the boundary layer for the duration of the plate assuming a laminar profile and associated friction velocity. The grid is also clustered to the start of the plate and then the streamwise spacing is relaxed to include roughly 50 points per wavelength of the specified second mode, resulting in a $\Delta x^+ = \Delta z^+ = 26$ streamwise and spanwise grid resolution. The outlet of the domain contained rapid growth in the streamwise cell sizes to act as a buffer layer and damp upstream traveling acoustic waves in the simulation. Thus, any items plotted beyond a streamwise location of $x = 0.54$ should be considered as non-physical due to the extreme stretching in the grid. A fourth order Runge-Kutta time integration was used to advance the flow approximately 6 flow-through times allowing the perturbations advecting from the inlet to reach a consistent maximum amplitude along the full length of the plate. The time-step used for the simulation allowed for 2000 steps per period of the fundamental temporal frequency.

The growth of the respective fluctuations are also compared to the growth anticipated from LST. The N-factor for

the fluctuation quantities from SPARC can be computed by the wall pressure perturbations RMS value by

$$N = \int_{x_0}^{x} \frac{1}{p'_{rms}} \frac{dp'_{rms}}{dx}\, dx + C. \tag{15}$$

Here, the C coefficient is used to shift the growth lines for comparison against the growth computed using LST from STABL as shown in Equation 27. The x_0 value is now taken as an initial streamwise location at the inflow. Since this is a linear growth analysis, this type of vertical shift can be used for comparison purposes only.

1. Dissipative flux

For shock-capturing schemes by Subbareddy-Candler, shock capturing is accomplished by adding a dissipative flux [3] of the form

$$F'_{f,diss} = \alpha_{diss} D_f, \tag{16}$$

where the prime indicates the projection of a vector onto the unit normal vector at a face, f indicates the values calculated at a cell face. α_{diss} is the dissipation switch which takes on values near zero in smooth regions of the flow and values close to one at the shock. D_f is the dissipative portion of a standard shock capturing scheme and it has the form

$$D_f = -\frac{1}{2}(R|\Lambda|R^{-1})_f \cdot (U_{nbr} - U_i). \tag{17}$$

Where U_{nbr} indicates the state vector of the associated neighbor cell and U_i indicates the state vector of the current cell. Here, R is the right eigenvector matrix of the flux Jacobian $A = \partial F'/\partial U$, Λ is the diagonal matrix of eigenvalues of A, and U is the state vector of conserved variables in compressible flow.

If we take a periodic assumption for the slow acoustic mode $U_i = \overline{u} + \hat{u}(t)\sin(\alpha x)$, then the difference between the neighbor value and the i^{th} cell becomes

$$\begin{aligned} U_{nbr} - U_i &= \hat{u}(t)(\sin(\alpha(x + \Delta x)) - \sin(\alpha x)) \\ &\approx \hat{u}(t)(\sin(\alpha x) + \alpha \Delta x \cos(\alpha x) - \sin(\alpha x)) \\ &\approx \hat{u}(t)\alpha \Delta x \cos(\alpha x), \end{aligned} \tag{18}$$

using small angle approximation. Here, Δx indicates the local grid spacing in the streamwise direction, and α is the streamwise wavenumber. This equation states that the difference between the neighbor values and the i^{th} cell scales with $\alpha \Delta x$. Since we know the eigenvalue associated with A to be ω, we can then say the dissipation portion scales with this eigenvalue, or in other words

$$F'_{f,diss} = \alpha_{diss} D_f \sim -\frac{1}{2}\alpha_{diss}\alpha \Delta x \omega. \tag{19}$$

Using the phase velocity, we find that the magnitude of the dissipation should decay by

$$u'_{rms}(x) = u'_{rms}(x = x_0) e^{-\int_{x_0}^{x} \frac{1}{2}\alpha^2 \Delta x \alpha_{diss}\, dx}. \tag{20}$$

Here, Δx is a function of the grid spacing, thus the decay rate changes as the grid spacing changes.

The α_{diss} is also a function of the velocity shock-sensor technique. If one uses the Mach [13] dissipation-switch (sensor 1) then the dissipation can be calculated by

$$\begin{aligned} \alpha_{diss} &= \begin{cases} \frac{\Delta M^2 + \delta^2}{2\delta}\left(1 - e^{-\kappa M_a}\right) & \text{when } |\Delta M| <= \delta \\ |\Delta M| & \text{when } \delta < |\Delta M| <= 1 \\ 1 & \text{when } |\Delta M| > 1 \end{cases} \\ \Delta M &= M_L - M_R. \end{aligned} \tag{21}$$

Here, M_a is the arithmetic mean of left and right Mach numbers, the parameter $\kappa = 10$ is a good empirical value for supersonic cases, the parameter $\delta = 0.5$ is used for cases presented here. For a supersonic freestream periodic perturbation, the terms ΔM^2 and $e^{-\kappa M_a}$ are small and can be neglected, this leaves the minimum dissipation value for a freestream low-amplitude disturbance in supersonic flow as being the minimum value of

$$\alpha_{diss} = \frac{\delta}{2} = 0.25. \tag{22}$$

Shock sensor	Equation for α_{diss}	$\min(\alpha_{diss})$
Sensor 1 [13] using Equation 21	$\begin{cases} \frac{\Delta M^2+\delta^2}{2\delta}\left(1-e^{-\kappa M_a}\right) & \text{when } \lvert\Delta M\rvert \le \delta \\ \lvert\Delta M\rvert & \text{when } \delta < \lvert\Delta M\rvert \le 1 \\ 1 & \text{when } \lvert\Delta M\rvert > 1 \end{cases}$	$\frac{\delta}{2} = 0.25$
Sensor 2 [14] using Equation 23	$\min\left(\frac{\theta^2}{\theta^2+\omega^2+\epsilon}, 1\right)$	1
Sensor 3 [15] using Equation 25	$\max(\min\left(\frac{-\theta}{\frac{3}{2}\omega+a\epsilon}, 1\right), \alpha_{min})$	α_{min}

Table 3 Summary table of the shock sensor types used with the Subbareddy-Candler fluxes.

If α_{diss} is calculated from using another technique, such as the Ducros [14] shock detection switch (sensor 2), then

$$\alpha_{diss} = \min\left(\frac{\theta^2}{\theta^2+\omega^2+\epsilon}, 1\right). \tag{23}$$

Here, ω is the vorticity magnitude, θ is the divergence of the velocity, and ϵ is a small number to prevent division by zero. In a freestream location where small linear perturbations are present, the compressibility effects are dominant (represented by the dilatation) and thus the full magnitude of the dissipative flux is applied such that the minimum value is

$$\alpha_{diss} = 1. \tag{24}$$

In the boundary layer, however, vorticity magnitude increases and the dissipation magnitude becomes small. Thus, capturing the growth of a perturbation wave in a boundary layer one would expect only minor numerical dissipation due to this shock sensor. However, in the freestream, one would expect a significant amount of dissipation.

If α_{diss} is calculated from using a third technique such as a variation of the sensor from Reference [15] (sensor 3), then

$$\alpha_{diss} = \max(\min\left(\frac{-\theta}{\frac{3}{2}\omega + a\epsilon}, 1\right), \alpha_{min}). \tag{25}$$

Here, ω is the vorticity magnitude, θ is the divergence of the velocity, ϵ is a small number, and a is the speed of sound. In a freestream location where small linear perturbations are present, then the speed of sound term is large, thus the minimum dissipation is set by α_{min} for freestream location

$$\alpha_{diss} = \alpha_{min}. \tag{26}$$

In the boundary layer, the vorticity magnitude becomes larger, and again the α_{min} value is found in that region of the domain. This is advantageous as one has control over the added numerical dissipation in both the freestream and the boundary-layer due to the shock sensor. In some cases of low disturbances, α_{min} can be set to zero to minimize any extra dissipation outside of the shock location. It is observed, however, that setting α_{min} to zero does introduce some numerical difficulties where the solution can diverge if a good initial condition is not provided and some transient behavior is needed to be propagated through the domain before finding the steady-state solution.

The three shock sensors used in this work are summarized in Table 3. This shows the equation numbers for α_{diss} and the freestream minimum dissipation expected for a small amplitude disturbance.

IV. Results

The final state of the boundary layer and streamwise perturbations are shown in Figure 6 for a specific time instant for a 2D acoustic simulation. The other simulations have very similar qualitative appearance and are not shown for brevity. In this figure, we observe the growth of the boundary layer alongside the initiation and growth of the second mode instability. The colored circles in Figure 6 show the local maximum disturbance amplitude (in the wall-normal dimension) at a few specified streamwise locations. We take the FT at each of these locations and plot the magnitude of the coefficients as a function of the frequency. These colored circles match the colors of the FT coefficients shown in Figure 7 for those same locations.

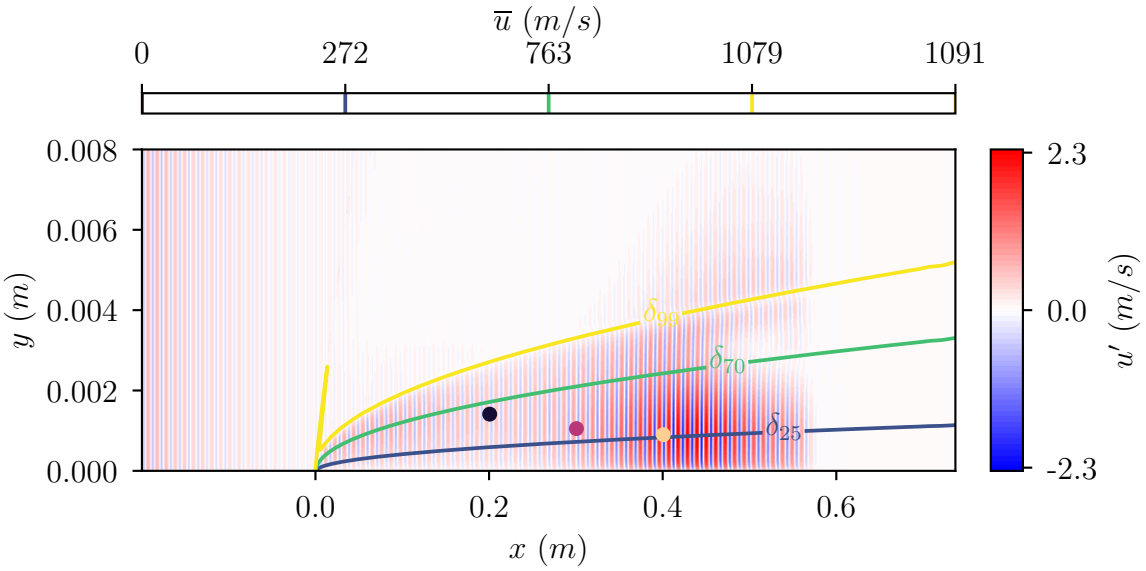

Fig. 6 DNS results using SPARC with a uniform periodic inflow condition. Contour lines show the average streamwise velocity at several boundary layer locations, colored domain shows streamwise perturbations at a single time instant. The colored dots indicate the maximum wall-normal streamwise RMS value at various streamwise locations. The colors of these dots match with the FT magnitude shown in Figure 7.

We can see the magnitude of the second harmonic in Figure 7 is orders of magnitude smaller than the fundamental harmonic, thus it shows that for these cases a linear assumption is an adequate approximation. Since the nonlinear coefficients are small, comparison to linear growth is acceptable here as the second harmonics don't alter the linear growth in a significant manner. It should also be noted that the other simulations had lower-amplitude fluctuations and thus were even more linear than this case as will be shown below. The following results will show similar plots and FT analysis for two case studies.

A. Case study: acoustic, 2D, and 3D

The results and simulations presented in this case study were presented previously in [6] and are highlighted here again for the reader. A comparison of the RMS of the streamwise fluctuation for the acoustic inflow simulation, the 2D eigenfunction inlet simulation, and a 3D eigenfunction inlet simulation can be seen in Figure 8. This figure also presents a good visual of the three separate inflow locations. The vertical colored lines identify the various streamwise locations where the second mode from STABL is compared to the FT fundamental harmonic of the matching frequency. Figure 9 shows the magnitude of the FT coefficients at the indicated locations.

Figure 10 shows how the shape of the FT fundamental mode in the SPARC simulations compares well to the shape of Mack's second mode from STABL at various streamwise locations. We note here, that the magnitude of the individual modes needed to be scaled for proper qualitative comparison. It is also observed that the magnitude of the fundamental harmonic far from the boundary layer in the 2D acoustic simulation at a streamwise location $x = 0.046$ is much higher than what is predicted by LST while still resembling the second mode in the boundary layer. This is due to the fact that our inlet to this simulation is uniform in the wall-normal direction and retains some magnitude at locations far from the boundary layer. However, as one moves further downstream, we observe that this acoustic mode dissipates away far from the boundary layer and matches the LST prediction. Additionally, the 3D BL inlet profile at $x = 0.26$ seems to retain some transient behavior as it doesn't match what the LST predicts that well, however, as one moves further downstream we see that it collapses back to the expected shape. This shows that after an initial transient behavior, that the BL inlet allows for excellent agreement between LST and DNS simulations using SPARC.

The N factor is an estimate of the growth of the perturbation magnitude and can be used as an indicator for transition scenarios. This N factor is estimated using PSE from the kinetic energy of the perturbation integrated along the

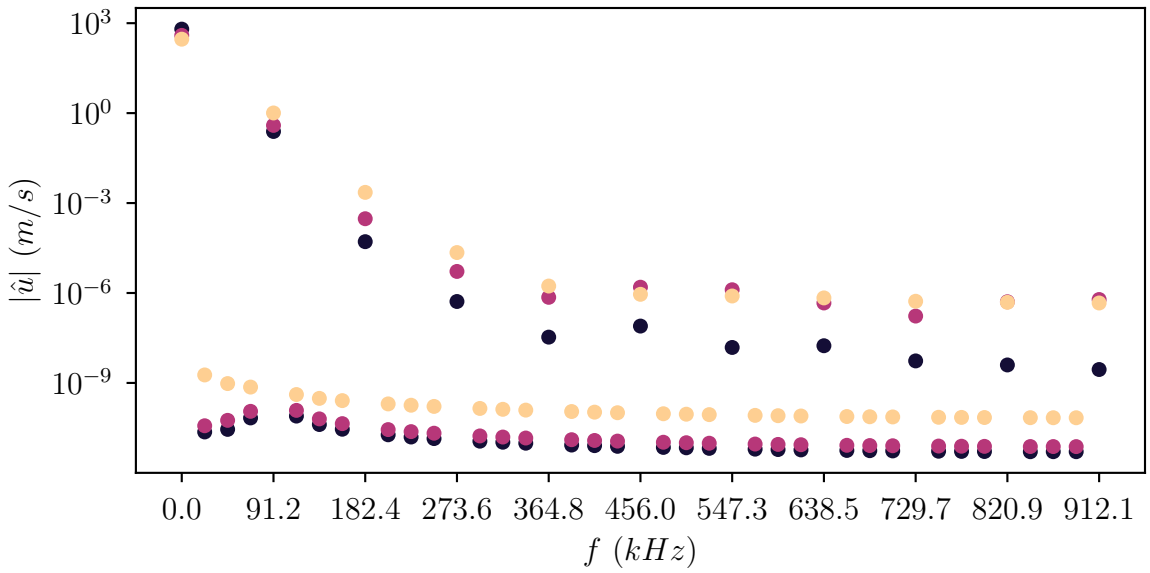

Fig. 7 FT coefficients in time as a function of temporal frequency of the DNS results using SPARC. The colored dots match with the dots and locations shown in Figure 6 for the simulation domain.

wall-normal direction along with the growth rate integrated across the streamwise direction as

$$\sigma = -\alpha_i + \frac{1}{E}\frac{dE}{dx}, \tag{27a}$$

where

$$E = \int \overline{\rho}(|\hat{u}|^2+|\hat{v}|^2+|\hat{w}|^2)d\Omega, \tag{27b}$$

and

$$N = \int_{x_0}^{x} \sigma\, dx. \tag{27c}$$

For the DNS calculations, the values of C for each case in Equation 15 is presented in Table 4. This same shifting is

Case	C	Case	C
2D acoustic	2.402	2D BL inlet	0.934
3D BL inlet	-1.408	Sensor 1, SPARC inflow	1.01
Sensor 3, acoustic inflow	-1.064	Sensor 2, acoustic inflow	6.718
Sensor 1, acoustic inflow	2.157	Sensor 2, STABL inflow	-1.519

Table 4 Table of C coefficient values for each DNS case as presented in Figures 11, 18, and 20.

done in all following N-factor plots. Since DNS contains nonlinear calculations, this kind of shifting is not proper, but is used for comparison purposes only.

Comparing the respective growth for the simulations and LST, in Figure 11, shows good agreement except for the acoustic inflow simulation, which experiences less growth. This is due to the different dissipation switch used in this simulation. The acoustic inflow case utilized the Mach dissipation switch [16] (sensor 1). The BL inlet simulations utilized the second shock-sensor (sensor 2) [14] dissipation switch. The minimum dissipation level of the Mach switch is noticeably higher than that of the sensor 2 switch in the boundary layer. It is most likely that this increase in dissipation led to the lower growth rate observed in the acoustic simulation, but not in the other simulations. The initial transient at the two eigenfunction inflow simulations can be observed, but the main growth of the second mode is easily comparable across all simulations with the exception of the acoustic inflow simulation.

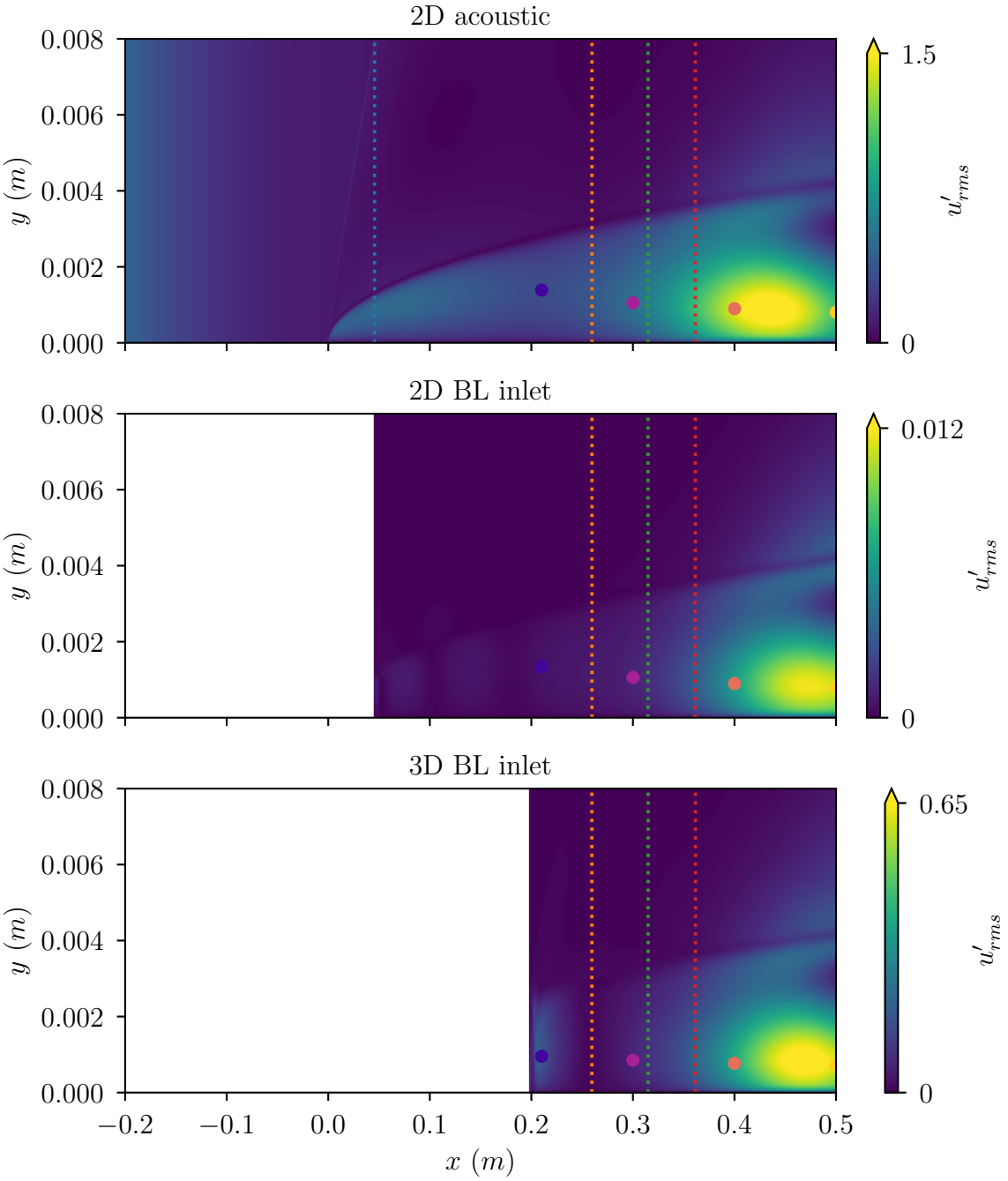

Fig. 8 DNS results using SPARC for the three simulations of the streamwise RMS of the fluctuation. The top acoustic case has the largest upstream domain. The vertical colored lines indicate the locations that match the colored lines in Figure 10.

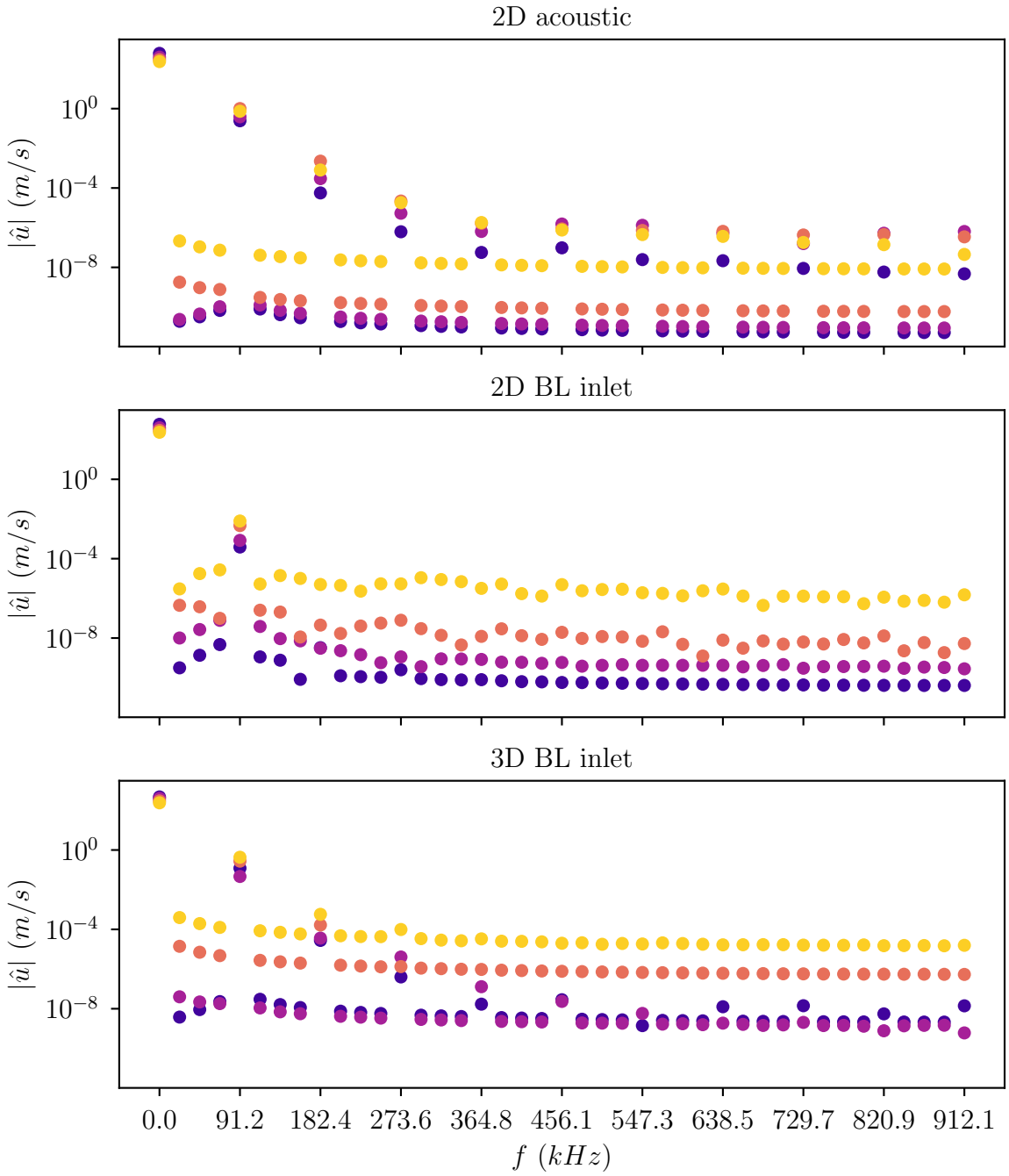

Fig. 9 Streamwise FT coefficient magnitude at the matching colored dots from Figure 8.

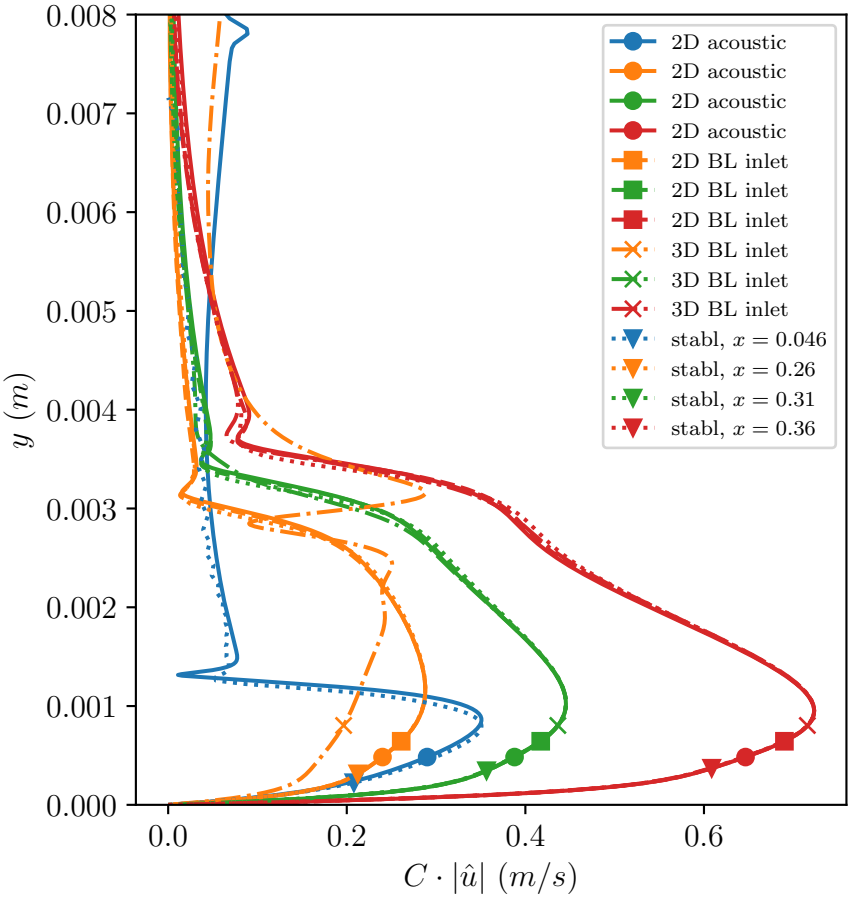

Fig. 10 Fundamental frequency of the streamwise velocity FT from DNS results using SPARC for the third case study shown in Section IV.A. This is compared to the eigenfunction at the same streamwise locations as computed using STABL. The color of the lines match the streamwise location of the vertical colored dotted lines shown in Figure 8.

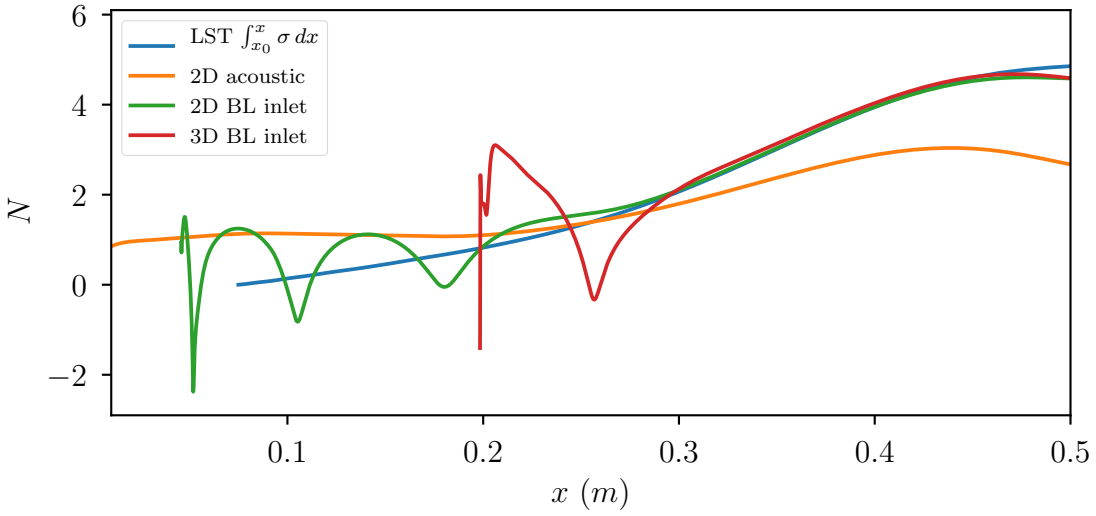

Fig. 11 STABL largest instability mode predicted N-factor compared to the N-factor from the DNS simulations. The frequency is 91.2 kHz **and spanwise wavenumber is** $\beta = 0/\mathrm{m}$**.**

B. Case study: Shock-capturing and inflow boundary

We now turn our attention to comparing several DNS studies to LST and some previous results in [6]. A few remaining questions in [6] are further investigated in the present study.

First, the initial inflow boundary condition seemed to yield an undesirable transient region in DNS. The inflow condition in that prior work used a pure eigenfunction as calculated using STABL [4]. A modification to this boundary condition is used where the Fourier transform is taken from a previous 2D simulation and is used as the inflow condition to the next simulation. This is similar to the 2D eigenfunction inflow condition, just with a change in the shape of the baseflow and associated shape function. It was shown that the shape of the disturbances in these two cases are very similar. However, as it will be shown, it has a significant impact on the initial transient at the inflow condition. This is largely due to the small differences in baseflow and the resulting eigenfunction from STABL. These small differences is what causes the small transient behavior before the true second mode becomes the dominant growth mechanism observed in the N-factor plots.

The baseflow at $x = 0.046$ is shown in Figures 12, 13, 14, 15, and 16. These figures show fairly good agreement between the streamwise velocity and temperature. However, small subtle differences are observed when the density, wall-normal velocity, and pressure are compared. The wall-normal velocity in Figure 14 shows a small deviation near the boundary layer edge and above $y = 0.007\ m$. This was the edge of the STABL simulation domain at this streamwise location and so a constant valued extrapolation was used for values above this point when given as an inflow condition for SPARC. It is expected that this small difference at this wall-normal distance would have a relaxation distance based on the Mach angle of 6 cm before it impacted the growth rate and shape near the wall. Therefore, this difference in inflow condition is not the leading cause of the initial transient behavior in the near-wall region at the beginning of the DNS studies. The pressure in Figure 16 shows a small pressure pulse when using the STABL solution around $y = 0.0012\ m$. This small pressure pulse in the near-wall region also impacted the eigenfunction and disturbance quantities in that vicinity as can be seen in Figure 17. We see there that the pressure is drastically different at the same wall-normal location between the 2D acoustic case and STABL, which may be the reason for the significant wall-normal velocity change during the initial transient period when using a STABL inflow condition. Thus, future investigations must have smoother baseflow profiles to obtain more accurate eigenfunction inlet profiles before they can be used to accurately capture second mode growth. A change to a previous SPARC simulation as an inflow condition also utilizes the smoother profiles and eliminates the extra pressure pulse leading to the transient behavior.

The second question investigated had to do with the excessive damping that occurred when the dissipation switch was altered. A series of DNS studies were then performed to investigate three separate dissipation switches along with a few parameters.

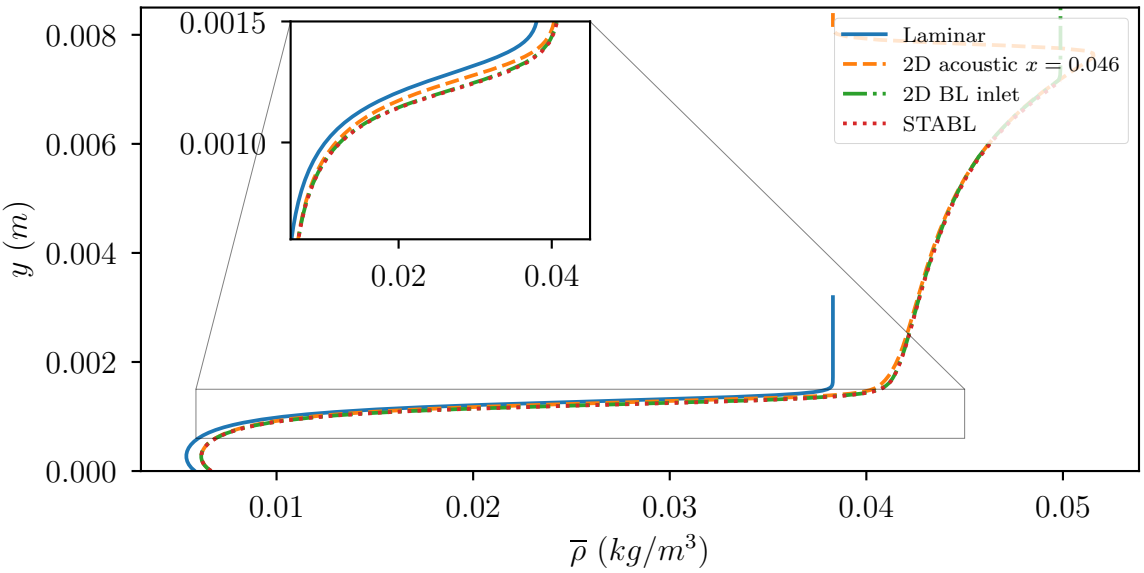

Fig. 12 Baseflow density at $x = 0.046$ from the Laminar similarity solution, 2D acoustic inflow DNS from section IV.A, 2D BL inlet DNS from section IV.A, and from STABL. The 2D BL inlet case uses the STABL solution as the inflow boundary condition, what is plotted here as the 2D BL inlet is the first interior cell solution.

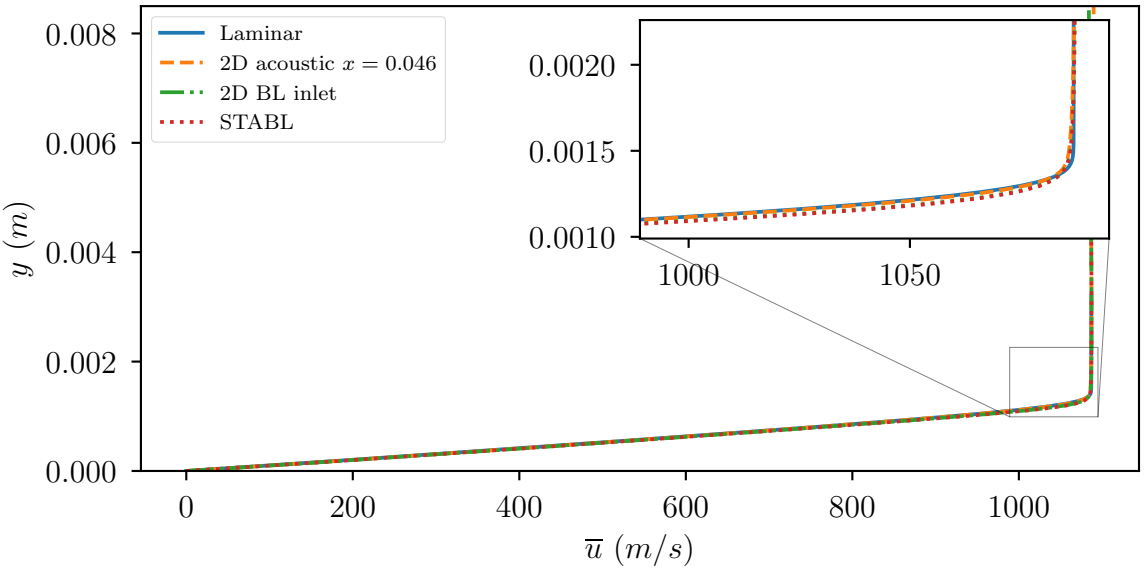

Fig. 13 Baseflow streamwise velocity at $x = 0.046$ from the Laminar similarity solution, 2D acoustic inflow DNS from section IV.A, 2D BL inlet DNS from section IV.A, and from STABL.

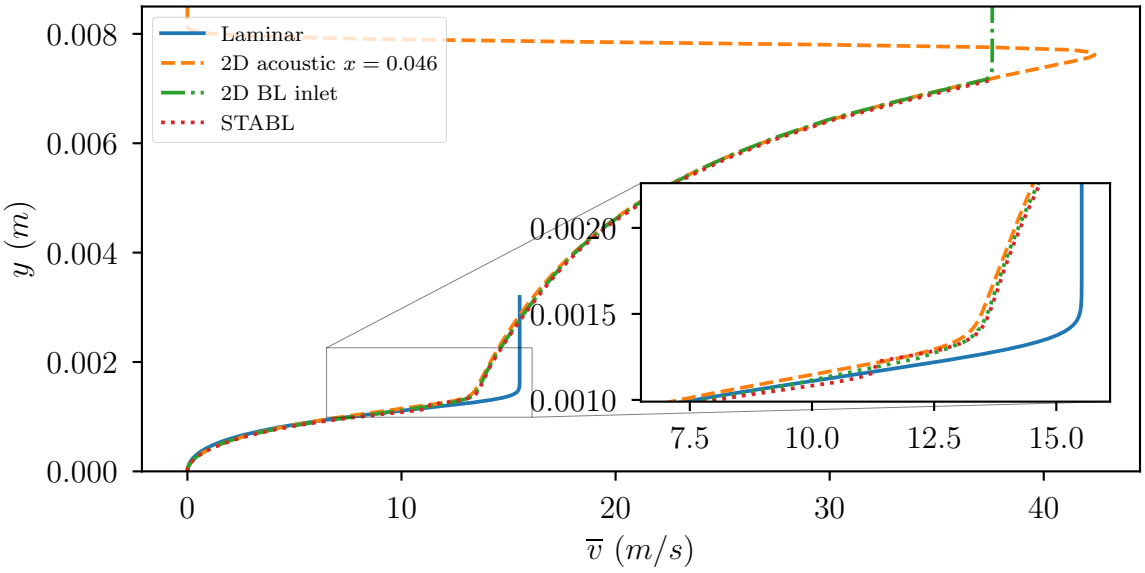

Fig. 14 Baseflow wall-normal velocity at $x = 0.046$ from the Laminar similarity solution, 2D acoustic inflow DNS from section IV.A, 2D BL inlet DNS from section IV.A, and from STABL.

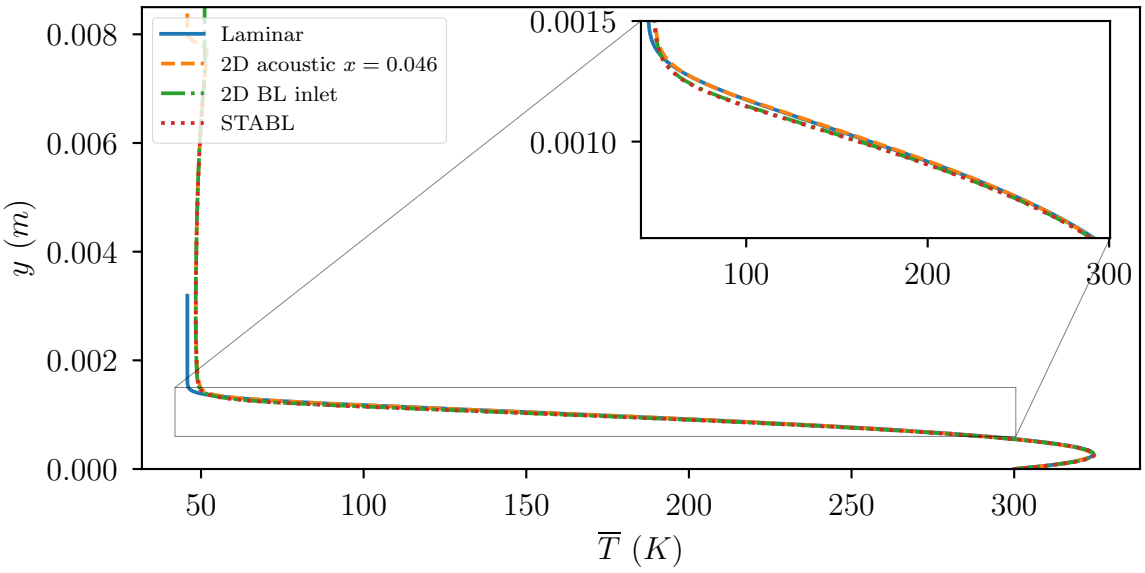

Fig. 15 Baseflow temperature at $x = 0.046$ from the Laminar similarity solution, 2D acoustic inflow DNS from section IV.A, 2D BL inlet DNS from section IV.A, and from STABL.

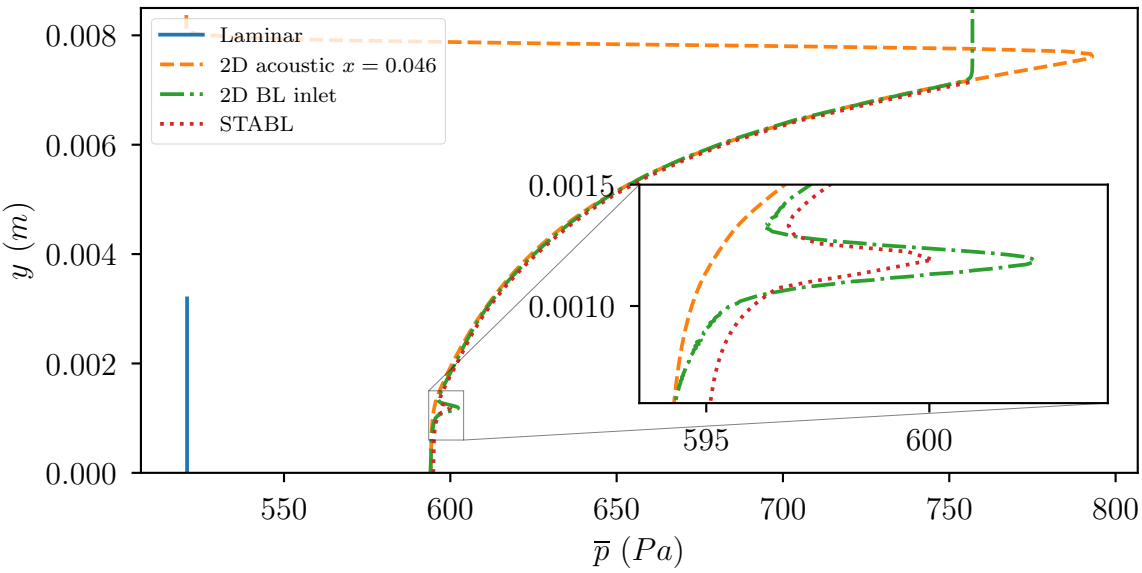

Fig. 16 Baseflow pressure at $x = 0.046$ from the Laminar similarity solution, 2D acoustic inflow DNS from section IV.A, 2D BL inlet DNS from section IV.A, and from STABL.

1. N factor growth

Using the wall-pressure root mean square, we can calculate the magnitude of the *N* factor. The *N* factors are shown in Figures 18 and 19 for four DNS cases and is compared to the STABL LST calculation. The 'acoustic inflow' indicates that the inflow condition is a simple uniform slow acoustic mode as described in [6]. The 'SPARC inflow' case indicates that a previous 2D simulation was run, and the output was extracted and used at a location $x = 0.22$ downstream of the leading edge of the flat plate and used as an inflow condition.

Since N factor is calculated using the wall-pressure, the local numerical dissipation from the shock sensor should be small or non-existent for all three sensors used. However, as shown in Figure 18, the Mach sensor (sensor 1) adds a significant amount of extra numerical dissipation to the disturbance in the boundary layer. This holds for both of the inflow boundary conditions used. Sensor 2 and sensor 3, on the other hand, both capture the entire amplitude growth of the second mode quite well. This shows that these two sensors do not add any excessive numerical dissipation in the boundary layer.

Figure 20 adds an additional DNS case than was presented previously in Figures 18 and 19 that uses the inflow condition from STABL. Here, the transient behavior can be compared when using an inflow condition from STABL or an inflow condition from a previous simulation using SPARC. We can see that using a previous SPARC simulation nearly removes the transient behavior altogether. This result suggests that significant care must be taken when using different numerical results. STABL utilizes a separate baseflow solver and disturbance eigenfunction. The SPARC simulation uses consistent discretization accuracy and terms from the governing equations. These small differences in the baseflow and disturbance shape is what led to the observed transient behavior discussed previously and shown in Figure 20.

2. Freestream disturbances

We now turn our focus to dissipation of the disturbances in the freestream. As stated in Section III.B.1, in high Reynolds number cases, the inviscid Euler equations are applicable and we only observe minor dissipation in freestream acoustic modes. However, due to numerical dissipation owing to shock capturing techniques, one may introduce significant decay to freestream disturbances when using a numerical method. This decay will be dependent on the grid spacing used. This streamwise grid spacing for the 2D acoustic cases is shown in Figure 21 and 22. As discussed earlier, we retain roughly 50 discrete control volumes per wavelength of the fundamental mode. Near the leading edge of the flat plate, that increases to 500 points per wavelength.

A bank of simulations were run with various values for α_{min} while using sensor 3 dissipation switch. This switch allows for any value defined by the user. In complex settings, it may be useful to introduce some finite numerical dissipation for numerical stability. In one case, we can completely suppress the dissipation by setting $\alpha_{min} = 0$. We can

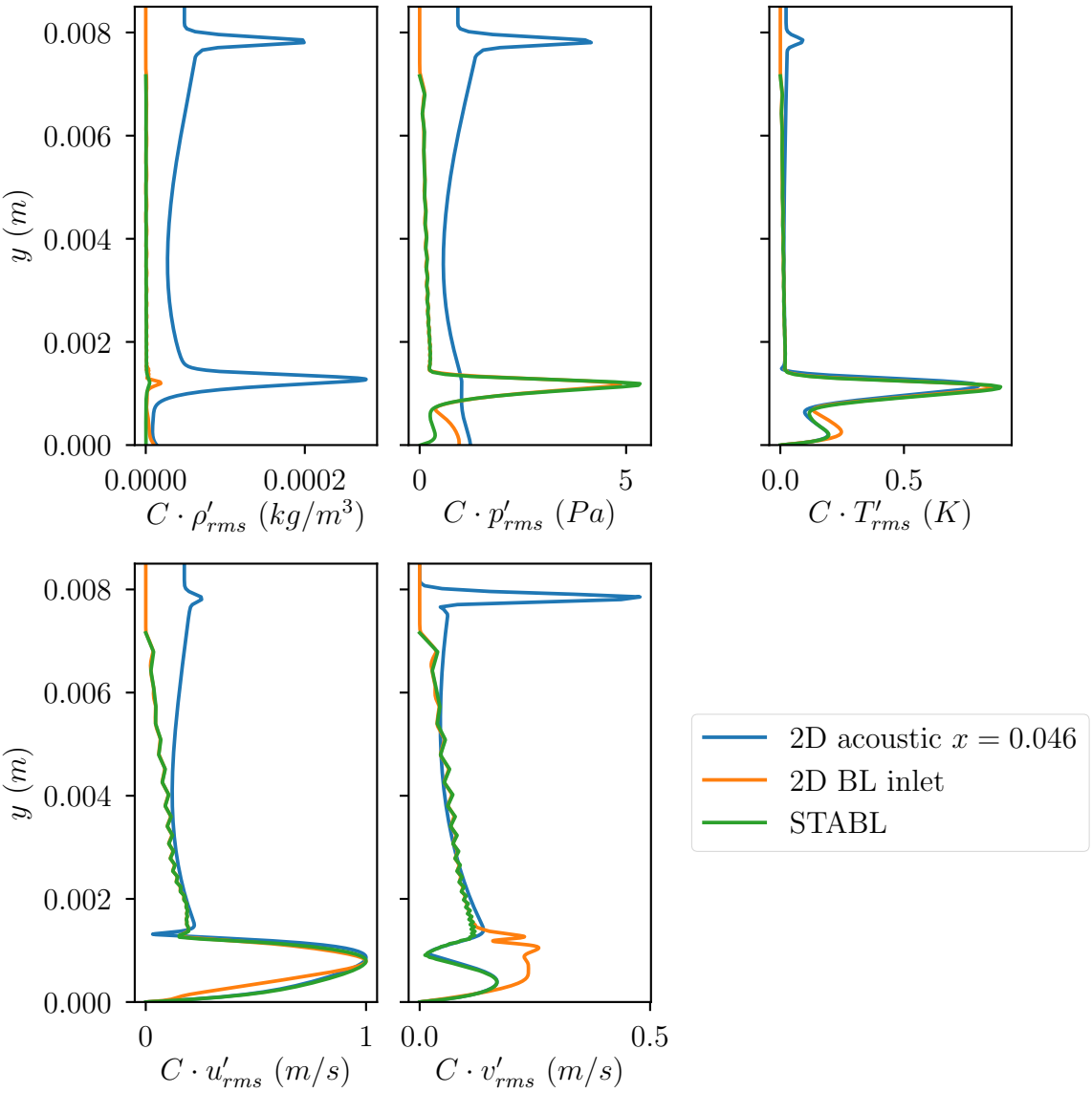

Fig. 17 Disturbance root mean square of the state at $x = 0.046$ comparing the 2D acoustic inflow DNS from section IV.A, 2D BL inlet DNS from section IV.A, and STABL solutions. Each state vector is normalized by a generic coefficient C such that the peak streamwise RMS quantity is unity. The 2D BL inlet cases uses the STABL values as the inflow boundary condition, but the plot shows the results from the first interior control volume.

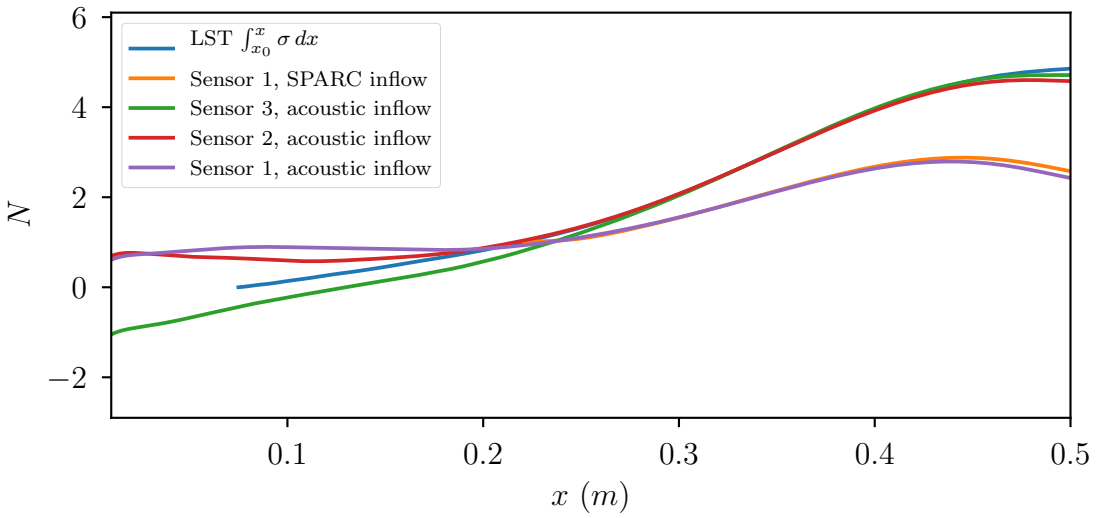

Fig. 18 *N* **factor growth of the DNS cases compared to LST. The magnitude of the DNS results were shifted in the vertical axis to match the values downstream of** $x = 0.2$**. This allowed for fairer comparison of the rapid growth region,** $0.2 < x < 0.4$**.**

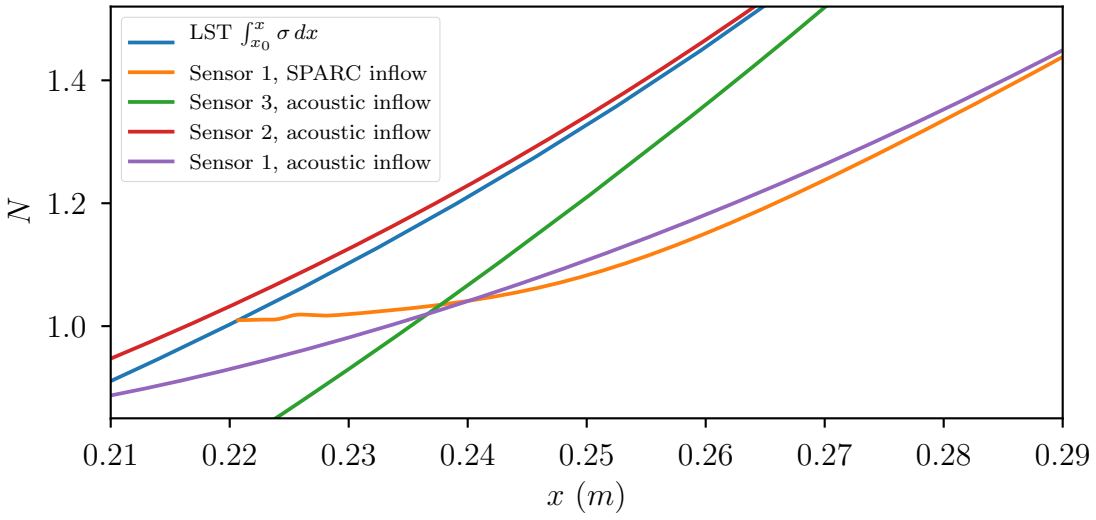

Fig. 19 Zoomed portion of Figure 18 to highlight the SPARC inflow solution.

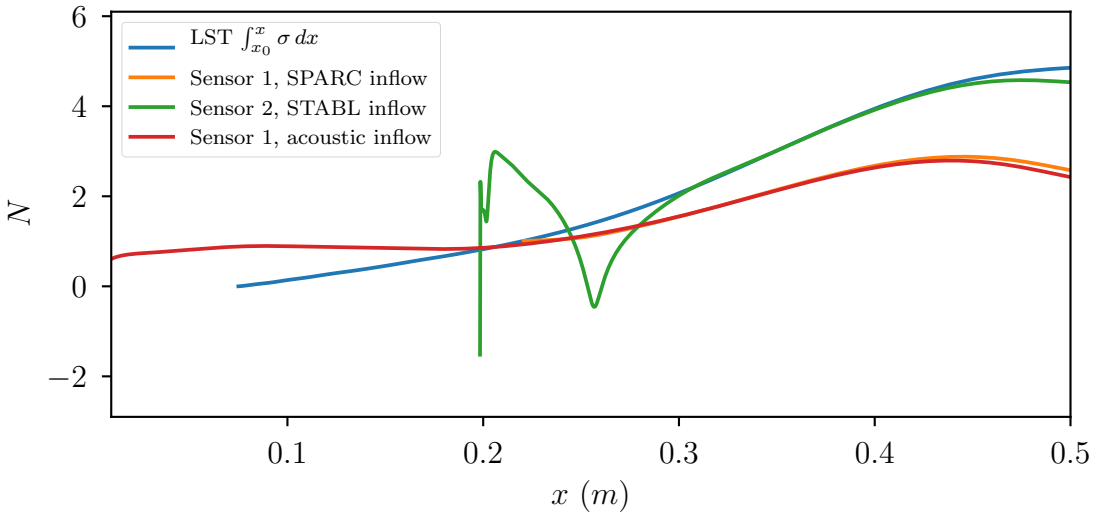

Fig. 20 *N* **factor growth of the DNS cases. This compares an earlier 3D case that used the baseflow and second mode eigenfunction calculated from STABL using the sensor 2 dissipation switch. The more recent 3D DNS case used a Mach dissipation switch (sensor 1) with an inflow calculated from a previous 2D SPARC simulation with a uniform acoustic inflow condition.**

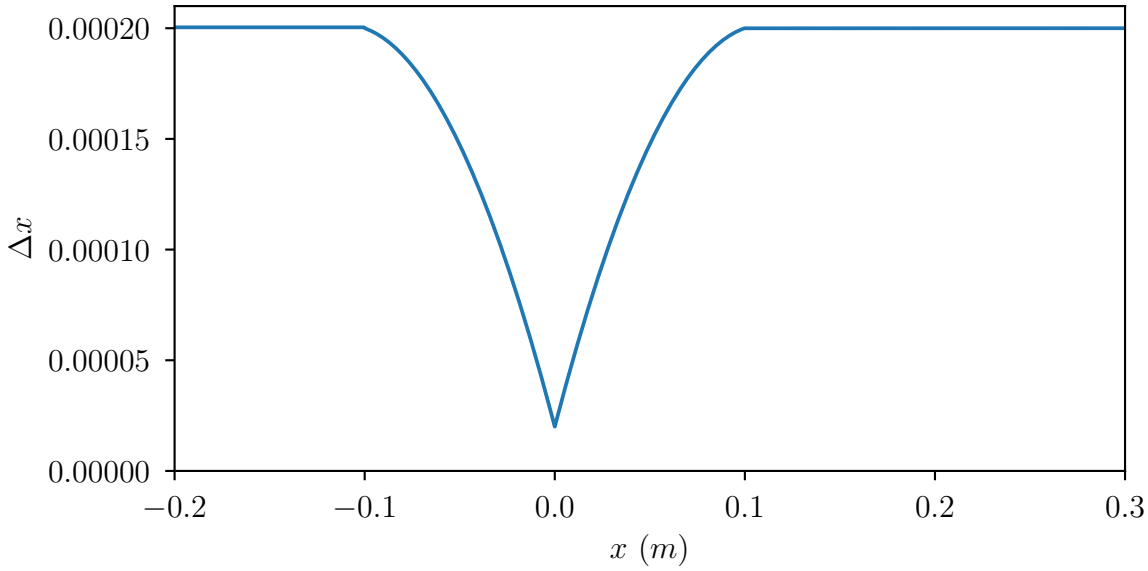

Fig. 21 Streamwise grid spacing in the streamwise direction for the 2D acoustic cases. The grid was refined near the leading edge of the flat plate.

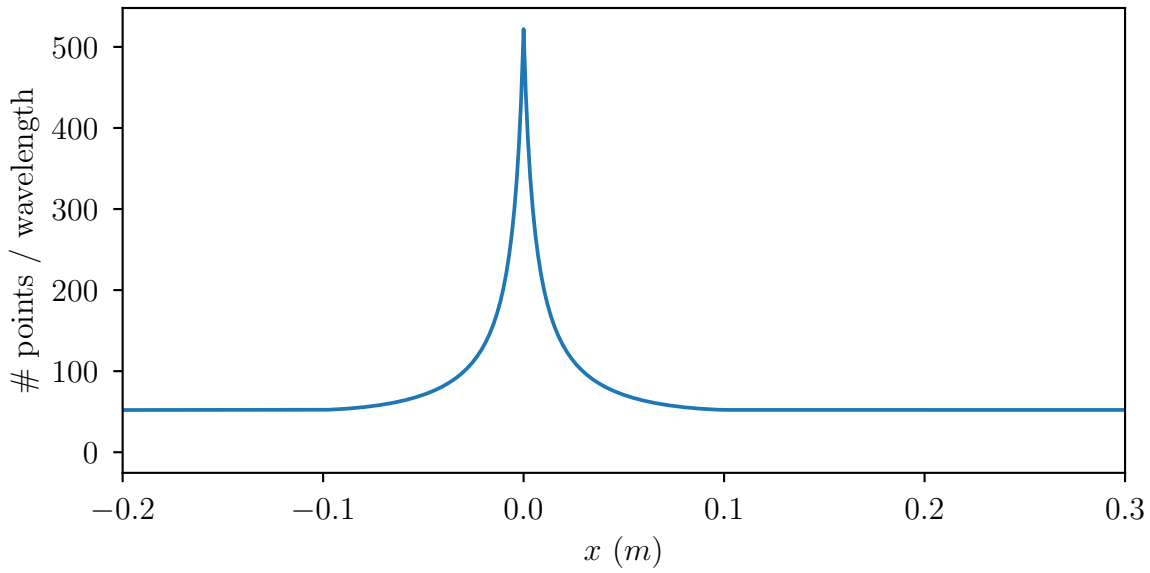

Fig. 22 Streamwise grid spacing in the streamwise direction for the 2D acoustic cases plotted as the number of points per the fundamental wavelength in the streamwise direction.

observe that the freestream disturbance theoretically has very negligible dissipation. The decay rate expected from LST nearly matches the observed decay from the simulation when we use sensor 3 with zero minimum dissipation (no added dissipation when no shock is sensed). Sensor 3 cases are shown in Figures 23 and 24 and compared to LST and the anticipated numerical decay due to the shock-capturing techniques.

When we use sensor 3 with a finite minimum dissipation, we observe significant numerical dissipation introduced throughout the domain. These figures also show the anticipated freestream numerical dissipation introduced by using the inviscid flux and dissipation switch of sensor 3. The anticipated decay due to grid spacing (see Equation 20) and the switch used in each case is shown to have excellent agreement with the resulting decay. The minimum α_{diss} values used in Equation 20 for each case are shown in Table 3 for the freestream disturbances. Figure 25 shows several other cases where the dissipation switch is changed to sensor 3 with values of α_{min} as either 0 or 0.2, the sensor 2 switch where the minimum freestream dissipation would be $\alpha_{diss} = 1$, or the Mach switch (sensor 1) where the minimum freestream dissipation would be $\alpha = 0.25$. Again, we see excellent agreement where we have cases that are two-dimensional and use the acoustic inflow condition. Additionally, a three-dimensional case that uses the Mach switch (sensor 1) with an inflow condition from a previous 2D acoustic case shows fairly good agreement between the expected numerical dissipation and the simulation.

3. One-Dimensional freestream disturbances at various conditions

A final aspect of this investigation was to calculate the freestream disturbance decay at various discretizations, conditions, and numerics using sensor 3. Additionally, a linearized solver [17] (labeled IO) was utilized and compared to high-fidelity simulations and compared to this inviscid theory (see Equation 20). Seven cases were run with the various parameters outlined in Table 5. Each case has two simulations (one high-fidelity DNS and one lower-fidelity linearized simulation) and one inviscid theory estimate (see Equation 20) for the numerical dissipation in a one-dimensional freestream flow.

The high-fidelity direct numerical simulation (DNS) was conducted by solving the full unsteady compressible Navier-Stokes equations with a time-varying and periodic acoustic mode superposed over the uniform inflow conditions using SPARC [2]. The grid retained significant stretching at the outflow to reduce any noise in the solution. This same grid was also used for the linearized solver. The linearized solver requires solving a steady state solution that only contains the uniform steady-state inflow condition. Then the solve for the time-periodic mode at the specified frequency is conducted to obtain the complex valued solution in the domain. The details of this direct solve are discussed in [17] and are labeled by input-output (IO) in the following figures. This IO solver is significantly faster and less costly than the high-fidelity DNS. It should be noted, however, that though this is part of the larger input-output optimization routine,

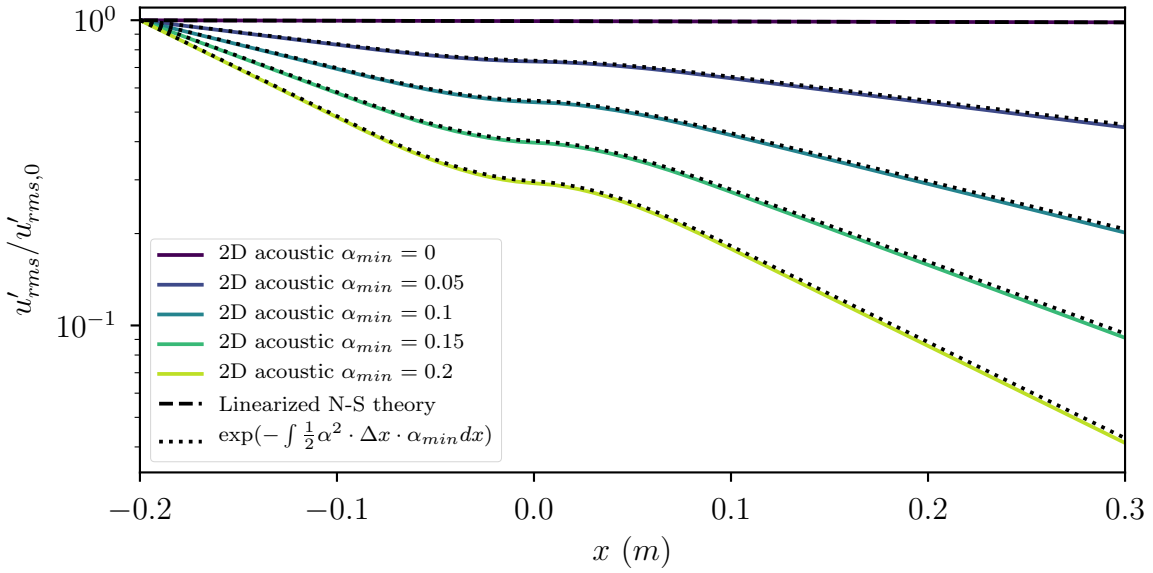

Fig. 23 Decay rate of the freestream acoustic mode from several DNS studies using sensor 3 dissipation switch with various α_{min} values. For all cases, the agreement between the decay expected from Equation 20 and the simulation disturbances is excellent.

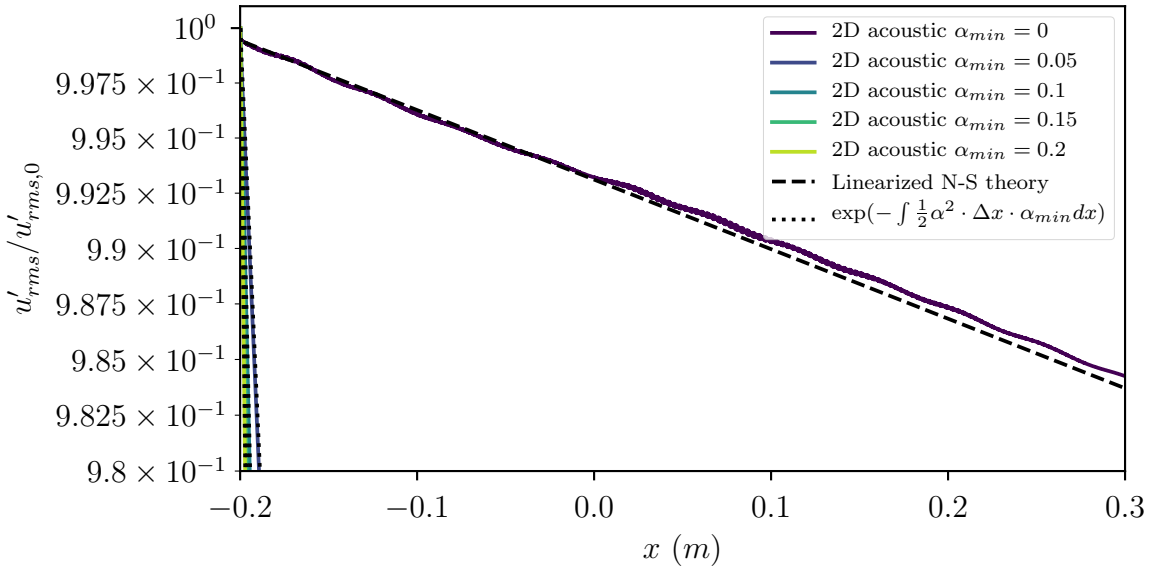

Fig. 24 Decay of the freestream acoustic mode from several DNS studies using sensor 3 dissipation switch with various α_{min} values, the vertical axis is zoomed to view the α_{min} = 0 and LST. Excellent agreement between LST and sensor 3 switch case is observed.

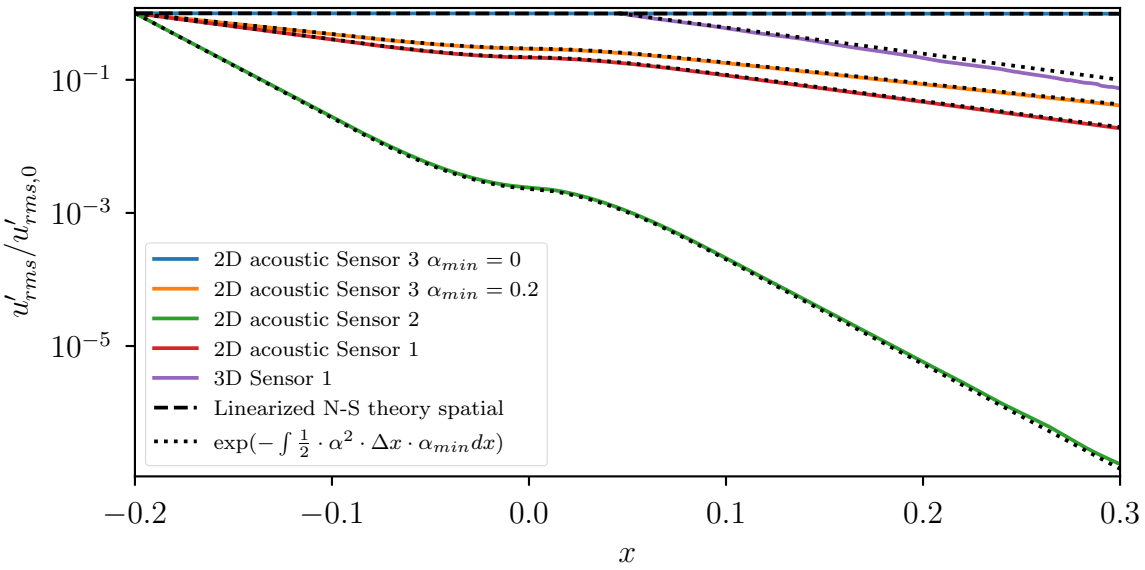

Fig. 25 Decay of the freestream acoustic mode for several DNS studies using the sensor 3, sensor 2, and Mach (sensor 1) dissipation switches. For all cases, the agreement between the decay expected from Equation 20 and the simulation disturbances is excellent.

only one forward direct solution was conducted on the acoustic mode in this work. This allowed for direct comparison to the high-fidelity DNS simulation that had low-amplitude periodic acoustic mode at the inflow. The third solution for each case is the inviscid theory presented in the previous sections in Equation 20. These results are shown in Figures 26 and 27. We see excellent agreement between all of the cases presented for the RMS of each disturbance quantity.

One interesting case performed was Case 6. In this case the steady-state solution for the linearized solver used a larger minimum dissipation value (α_{diss} = 0.2) in an effort to obtain the stead-state solution sooner. Since there are no disturbances in this freestream 1D case it yielded faster convergence with no loss of accuracy. Then, the minimum dissipation was altered to the α_{diss} = 0.05 magnitude for the linearized solver. We see that the decay rate matches with the solution of Case 2 where the dissipation value was consistent in both the steady state solution and in the linearized solution. This type of splitting of baseflow and linearized solver allows for optimal conditions for capturing the baseflow in an efficient manner as well as obtaining the linearized solution with minimal numerical dissipation.

The solution presented earlier in this article was for a first order reconstruction at each cell face. This means that the $U_{nbr} - U_i$ is the difference in the state vectors at the cell boundaries between two cells. However, if we were to use a second order reconstruction, we would incorporate gradient information for each cell. In this case of freestream disturbances the second order reconstruction uses a gradient away from each cell face to obtain the difference. Thus each velocity uses two cells that are away from the cell face of interest to obtain the estimated state at the cell face. Thus, a stencil of four cells are utilized for each face reconstruction (two for each side). Upon utilizing small angle approximation we obtain an estimation of zero added dissipation for an acoustic mode using the second order reconstruction. The result is shown in Case 7 and compared to first order reconstruction estimate at similar conditions shown in Figure 27 and shows very minimal dissipation compared to the first order counterpart.

V. Summary

Several simulations were conducted to understand two outstanding questions related to the compressible Mack's second mode from work presented in [6]. The transient behavior observed in the inflow region was solely due to the subtle differences in the numerical methods used to obtain the inflow fields using the two CFD solvers. When the inflow condition was changed to use data from the same CFD solver, the transient behavior disappeared. The second outstanding question had to do with the under-prediction of Mack's second mode in the boundary layer. It was shown that the excessive dissipation was due to the shock-capturing technique that led to the damped growth of the second mode. This numerical dissipation was both observed in the near-wall region as well as the freestream decay. An

Case	Number of points per period	α_{diss}	Inflow acoustic type	M	Order
1	50	0.2	Slow	9.8	1^{st}
2	50	0.05	Slow	9.8	1^{st}
3	25	0.2	Slow	9.8	1^{st}
4	25	0.2	Fast	9.8	1^{st}
5	25	0.1	Slow	4.9	1^{st}
6	50	0.2 then 0.05	Slow	9.8	1^{st}
7	25	0.05	Slow	9.8	2^{nd}

Table 5 Case and parameter descriptions for the one-dimensional freestream disturbances. The columns describe the Case identifier, the discretization of the number of points per period, the shock capturing numerical minimum dissipation values, type of inflow acoustic sent at the inflow, the Mach number, and the order of the reconstruction at the face locations.

expression for the simple decay rate due to numerical dissipation was derived and shown to be in excellent agreement for various minimum dissipation values and the three dissipation switches studied. Additionally, the one-dimensional freestream disturbance showed remarkable agreement for various parameters and conditions to the derived numerical dissipation and the linearized direct solve for a single aligned acoustic mode.

A. Illingworth Similarity Solution

The similarity solution to obtain the baseflow described in Section III.A is discussed in this appendix. The Illingworth transformation uses the stream function $\psi(x, y)$ as defined by

$$\frac{\partial \psi}{\partial y} = \rho u, \tag{28}$$

and

$$\frac{\partial \psi}{\partial x} = -\rho v, \tag{29}$$

where we can split the stream function using two similarity variables (ξ, η) as

$$\psi(\xi, \eta) = \int \rho u \, dy = G(\xi) f(\eta), \tag{30}$$

where

$$G(\xi) = \sqrt{2\xi}, \tag{31}$$

$$\xi = \int_0^x \rho_e(x) u_e(x) \mu_e(x) \, dx = \xi(x), \tag{32}$$

and

$$\eta = \frac{u_e}{G} \int_0^y \overline{\rho}(y') \, dy' = \eta(x, y). \tag{33}$$

The subscript e indicates a boundary layer edge quantity. For the cases we examine here, ξ can be further simplified to a zero-pressure gradient flow, or

$$\xi = \rho_e u_e \mu_e x. \tag{34}$$

We can also split the enthalpy using this similarity transformation as

$$h(x, y) = h_e(\xi) g(\eta). \tag{35}$$

Substitution of these terms into the momentum and energy equations assuming an ideal and perfect-gas assumption yields the coupled differential equation

$$(C f'')' + f f'' = \beta(f'^2 - g), \tag{36}$$

$$(Cg')' + \mathrm{Pr} f g' = \mathrm{Pr} C(\gamma - 1) M_e^2 f''^2, \tag{37}$$

where

$$\beta = \frac{2\xi}{M_e}\frac{dM_e}{d\xi}, \quad C = \frac{\rho\mu}{\rho_e\mu_e} \approx g^{n-1}. \tag{38}$$

For the zero-pressure gradient flat plate in a Nitrogen system, we can further reduce $\beta = 0$ and $n = 2/3$. The boundary conditions for the system are

$$f(0) = 0, \quad f'(0) = 0, \quad f'(\infty) = 1.0, \tag{39}$$

for the velocity at the wall and freestream and

$$g(0) = g_w, \quad g'(\infty) = 1.0, \tag{40}$$

for the isothermal boundary conditions. Once this solution is found by integrating the system, the physical quantities of interest can be found by the following relations. The density, streamwise and wall-normal velocities, and temperature are

$$\overline{\rho}(\xi, \eta) = \frac{\rho_e(\xi)}{g(\eta)} \tag{41}$$

$$\overline{u}(\xi, \eta) = u_e(\xi) f'(\eta), \tag{42}$$

$$\overline{v}(\xi, \eta) = -\frac{\sqrt{2\xi}\left(2\mu_e\rho_e x f + \sqrt{2\xi}(2x\int_0^y \frac{\partial\overline{\rho}}{\partial x}\, dy' - \int_0^y \overline{\rho}\, dy')f'\right)}{4\mu_e\rho_e x^2\overline{\rho}}, \tag{43}$$

and

$$\overline{T}(\xi, \eta) = T_e(\xi) g(\eta). \tag{44}$$

In order to obtain the wall-normal velocity, the expressions

$$y = x\sqrt{\frac{2}{Re_x}}\int_0^\eta g\, d\eta', \tag{45}$$

$$\frac{\partial\overline{\rho}}{\partial x} = -\frac{\rho_e\frac{\partial\eta}{\partial x}g'}{g^2}, \tag{46}$$

and

$$\frac{\partial}{\partial y}\left(\frac{\partial\eta}{\partial x}\right) + \frac{\sqrt{2}}{2}\frac{\rho_e u_e g'}{\sqrt{\xi} g^2}\left(\frac{\partial\eta}{\partial x}\right) = -\frac{\sqrt{2}}{4}\frac{u_e\overline{\rho}}{x\sqrt{\xi}}, \tag{47}$$

can be utilized. Here, Re_x is the Reynolds number based on the downstream location x. This similarity solution is solved at the conditions specified in Table 1 and presented in Figures 12-16.

Acknowledgments

The authors would like to thank Neal Bitter from Johns Hopkins Applied Physics Laboratory for the insights, feedback, and guidance regarding the LST, PSE, and DNS. They would also like to thank Jeff Fike and Michael Krygier at Sandia National Laboratories for the helpful discussions and guidance as well. Sandia National Laboratories is a multi-mission laboratory managed and operated by National Technology and Engineering Solutions of Sandia, LLC., a wholly owned subsidiary of Honeywell International, Inc., for the U.S. Department of Energy's National Nuclear Security Administration under contract DE-NA0003525.

References

[1] Fedorov, A., "Transition and Stability of High-Speed Boundary Layers," *Annual Review of Fluid Mechanics*, Vol. 43, No. 1, 2011, pp. 79–95. https://doi.org/10.1146/annurev-fluid-122109-160750, URL https://doi.org/10.1146/annurev-fluid-122109-160750.

[2] Howard, M., Bradley, A., Bova, S. W., Overflet, J., Wagnild, R., Dinzl, D., Hoemmen, M., and Klinvex, A., "Towards Performance Portability in a Compressible CFD Code," American Institute of Aeronautics and Astronautics (AIAA), 2017. https://doi.org/10.2514/6.2017-4407.

[3] Subbareddy, P. K., and Candler, G. V., "A fully discrete, kinetic energy consistent finite-volume scheme for compressible flows," *Journal of Computational Physics*, Vol. 228, 2009, pp. 1347–1364. https://doi.org/10.1016/j.jcp.2008.10.026.

[4] Johnson, H., and Candler, G., "Hypersonic Boundary Layer Stability Analysis Using PSE-Chem," 35th AIAA Fluid Dynamics Conference and Exhibit, 2005. https://doi.org/10.2514/6.2005-5023.

[5] Smith, J. A., DeChant, L. J., Casper, K. M., Mesh, M., and Field, R. V., "Comparison of a Turbulent Boundary Layer Pressure Fluctuation Model to Hypersonic Cone Measurements," American Institute of Aeronautics and Astronautics (AIAA), 2016. https://doi.org/10.2514/6.2016-4047.

[6] Harris, S., and Wagnild, R., "Second mode growth in a high-velocity boundary layer using stability theory and DNS," *AIAA Aviation 2021 Forum*, American Institute of Aeronautics and Astronautics, VIRTUAL EVENT, 2021. https://doi.org/10.2514/6.2021-2845.

[7] Illingworth, C. R., "Some solutions of the equations of flow of a viscous compressible fluid," *Mathematical Proceedings of the Cambridge Philosophical Society*, Vol. 46, No. 3, 1950, p. 469–478. https://doi.org/10.1017/S0305004100025986.

[8] White, F. M., *Viscous fluid flow*, McGraw-Hill New York, 1974.

[9] Johnson, H. B., Seipp, T. G., and Candler, G. V., "Numerical study of hypersonic reacting boundary layer transition on cones," *Physics of Fluids*, Vol. 10, No. 10, 1998, pp. 2676–2685. https://doi.org/10.1063/1.869781.

[10] Herbert, T., "Parabolized stability equations," *Annu. Rev. Fluid Mech.*, Vol. 29, 1997, pp. 245–283.

[11] Towne, A., Rigas, G., and Colonius, T., "A critical assessment of the parabolized stability equations," *Theoretical and Computational Fluid Dynamics*, Vol. 33, No. 3-4, 2019, pp. 359–382. https://doi.org/10.1007/s00162-019-00498-8.

[12] Bitter, N. P., "Stability of Hypervelocity Boundary Layers," Ph.D. thesis, California Institute of Technology, 2015.

[13] Jaisanker, S., and Raghurma Rao, S. V., "Diffusion regulation for Euler solvers," *Journal of Computational Physics*, Vol. 221, 2007, pp. 577–599. https://doi.org/10.1016/j.jcp.2006.06.030.

[14] Ducros, F., Ferrand, V., Nicoud, F., Weber, C., Darracq, D., Gacherieu, C., and Poinsot, T., "Large-Eddy Simulation of the Shock/Turbulence Interaction," *Journal of Computational Physics*, Vol. 152, No. 2, 1999, pp. 517–549. https://doi.org/10.1006/jcph.1999.6238.

[15] Larsson, J., Vicquelin, R., and Bermejjo-Moreno, I., "Large eddy simulations of the HyShot II scramjet," *Center for Turbulence Research Annual Briefs*, 2011, pp. 63–74. URL https://web.stanford.edu/group.ctr/ResBriefs/2011/06_larsson.pdf.

[16] Jaisankar, S., and Rao, S. R., "Diffusion regulation for Euler solvers," *Journal of Computational Physics*, Vol. 221, 2007, pp. 577–599. https://doi.org/10.1016/j.jcp.2006.06.030.

[17] Bitter, N., Kucala, A., Fike, J., Krygier, M., and Wagnild, R., "Coupling of Laminar-Turbulent Transition with RANS Computational Fluid Dynamics," Tech. Rep. SAND–2020-9914, Sep. 2020. https://doi.org/10.2172/1670532.

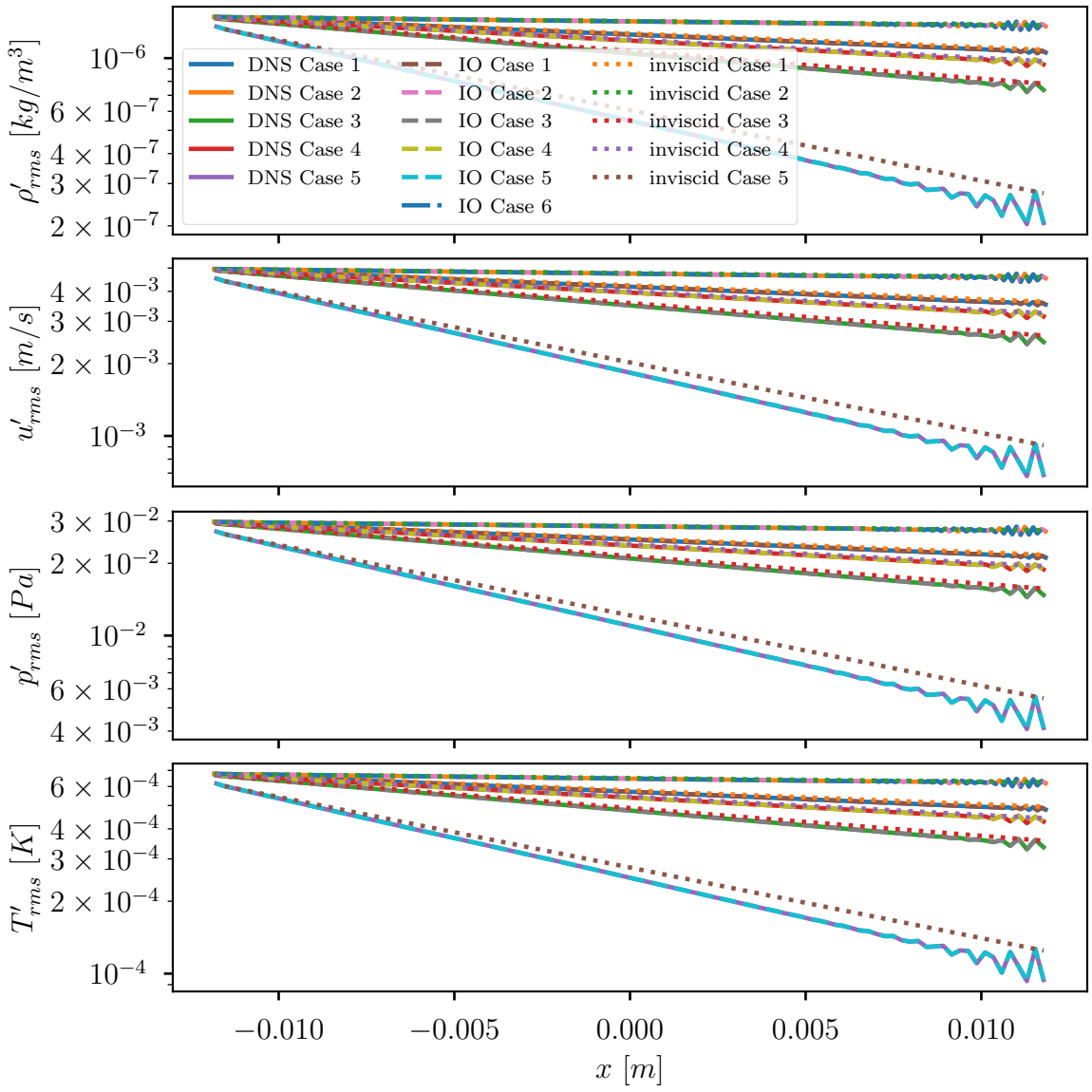

Fig. 26 RMS of the disturbances as calculated using high-fidelity simulations (DNS), linearized disturbance solver (IO), and the inviscid theory for the various parameters outlined in Table 5. We see excellent agreement between all three estimates for the RMS of the disturbances in a one-dimensional flow. Thus, the numerical dissipation introduced by the shock-capturing scheme yields the anticipated theoretical result and is matched in both the high-fidelity and linearized solvers.

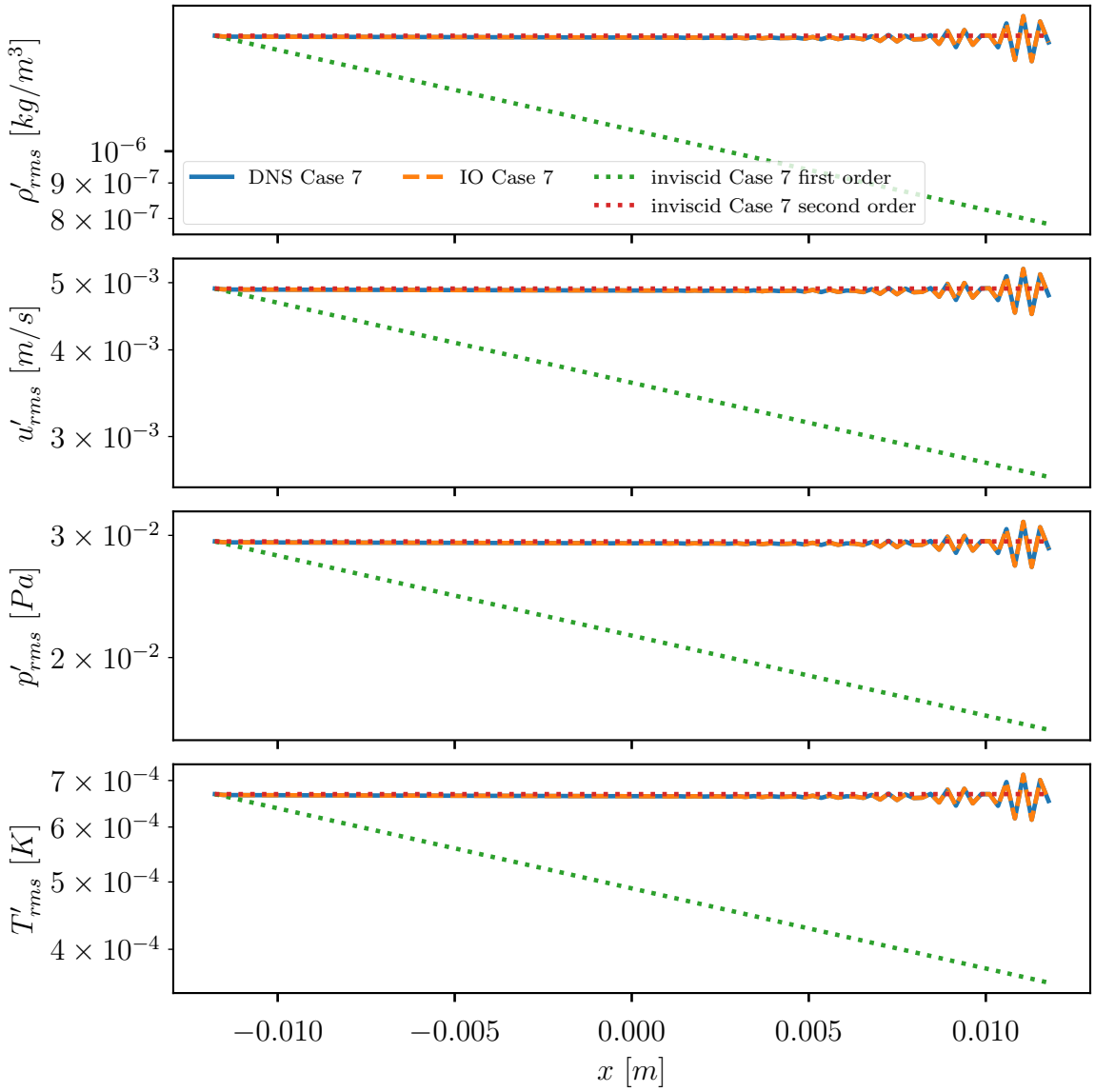

Fig. 27 Similar description as seen in Figure 26, except only outlining the seventh case. This case was special in that the inviscid theory predicted no added numerical dissipation for small amplitude acoustic modes using the second-order reconstruction. We observe here that using both the high-fidelity and linearized system we see very minimal numerical dissipation compared ot the first-order counterpart.